

Article

Mission Design and Orbit-Attitude Control Algorithms Development of Multistatic SAR Satellites for Very-High-Resolution Stripmap Imaging

Sangwon Lee ¹, Sang-Young Park ^{1,*}, Jeongbae Kim ², Min-Ho Ka ² and Youngbum Song ³

¹ Department of Astronomy, Yonsei University, 50 Yonsei-ro Seodaemun-gu, Seoul 03722, Republic of Korea

² School of Integrated Technology, Yonsei University, 85 Songdogwahak-ro Yeonsu-gu, Incheon 21983, Republic of Korea

³ Satellite System Division, Hanwha System, 491-23 Gyeonggidong-ro Cheoin-gu, Yongin 17121, Republic of Korea

* Correspondence: spark624@yonsei.ac.kr; Tel.: +82-2-2123-5687

Abstract: This study designs a multistatic synthetic aperture radar (SAR) formation-flying system for very-high-resolution stripmap imaging (VHRSI) using manufacturable SAR microsatellites. Multistatic SAR formation specifications for VHRSI are derived based on the SAR image theory. For the simultaneous multi-satellite operation, the advantages of the autonomous orbit and attitude control are prominent in terms of the workload of the ground station or the efficient performance of missions. Therefore, the autonomous relative-orbit-control algorithm using relative orbital elements is developed to maintain the designed multistatic SAR formation. Additionally, an autonomous attitude-control algorithm for multistatic SAR imaging is designed by applying the optimal right-ascension of the descending node (RADN) sector concept. Finally, the resolution improvement of VHRSI is verified through multistatic SAR imaging simulations. The multistatic SAR formation is designed with three satellites separated by 7.5 km each in the along-track direction. Autonomous relative orbit control maintains the relative position error within 45 m (3σ). Additionally, the autonomous attitude control simulation verifies that the satellites perform attitude maneuvers suitable for the operation mode, and the pointing error is maintained within 0.0035° (3σ). The spatial resolution of the multistatic SAR system for VHRSI is 0.95×0.96 m, which satisfies the very-high-spatial-resolution requirement.

Keywords: very-high-resolution stripmap imaging (VHRSI); multistatic SAR; satellite formation flying; relative orbit control; autonomous attitude control; optimal right ascension of descending node (RADN) sector



Citation: Lee, S.; Park, S.-Y.; Kim, J.; Ka, M.-H.; Song, Y. Mission Design and Orbit-Attitude Control Algorithms Development of Multistatic SAR Satellites for Very-High-Resolution Stripmap Imaging. *Aerospace* **2023**, *10*, 33. <https://doi.org/10.3390/aerospace10010033>

Academic Editor: Igor Belokonov

Received: 29 November 2022

Revised: 24 December 2022

Accepted: 27 December 2022

Published: 30 December 2022



Copyright: © 2022 by the authors. Licensee MDPI, Basel, Switzerland. This article is an open access article distributed under the terms and conditions of the Creative Commons Attribution (CC BY) license (<https://creativecommons.org/licenses/by/4.0/>).

1. Introduction

Unlike electro-optical (EO) satellites, synthetic aperture radar (SAR) satellites have the advantage of being able to image ground targets in cloudy conditions or at night because they use microwaves that are not affected by atmospheric conditions or light sources [1–4]. These all-weather and any-time capabilities can greatly help the national defense. The latest demand trends for SAR images, especially for reconnaissance in the national defense, are wide observation areas, short observation intervals, and high-resolution images [5,6]. The demand for wide-area observation and short revisit time can be satisfied through an appropriate constellation using multiple low-cost SAR microsatellites. The need for high-resolution SAR images, especially submeter level resolution in national defense, can be satisfied through X-band microwave and spotlight mode SAR imaging.

The concept of SAR, first proposed by C. A. Wiley in 1951, has continuously evolved [7,8]. Moreover, spaceborne SAR technology has advanced dramatically since 1978, after the Seasat was launched. Consequently, SAR satellites are used in various missions for earth observation, such as environmental investigation, ground mapping, disaster or traffic monitoring, and military reconnaissance [8–10]. In the 2010s, owing to material technology

advances and commercial off-the-shelf (COTS) developments, relatively inexpensive micro-class SAR satellites were manufactured [11–13]. Accordingly, commercial companies such as ICEYE, Capella space, and Synspective have developed SAR microsatellites, and they are providing high resolution (1~5 m) SAR images commercially [8,11,14].

Spotlight mode imaging cannot observe a wide area due to the narrow swath width and discontinuous imaging techniques [1,4]. Methods such as sliding spotlight mode were proposed to widen the observation area while maintaining a high resolution, but continuous SAR imaging was physically impossible in monostatic SAR systems [4,15]. Lopez-Dekker et al. [1] introduced a multistatic SAR concept that can overcome the limitations of monostatic SAR systems for azimuth resolution. Recently, various multistatic SAR missions performed by two or more SAR satellites have been actively investigated because they can increase the dimension of the measurement space or improve the signal-to-noise ratio [1,2,5,16,17]. The multistatic SAR system using a cross-track formation can produce accurate tomography, a three-dimensional (3D) map, and a digital elevation model (DEM) through single-pass interferometry [1,16]. Furthermore, multistatic SAR systems using along-track formation can provide functions such as ground moving target indicator and high-resolution wide swath [1,5]. These missions are either impossible or technically difficult with a single SAR satellite due to several limitations, such as spacing between channels and complex beamforming [1].

Although the concept of multistatic SAR for resolution enhancement has been presented, no research has been conducted on the system design level of the multistatic SAR for very-high-resolution (<1 m) SAR images. Therefore, among the currently operating SAR satellites, none is capable of continuous very-high-resolution imaging [18]. Various restrictions arise when the ground station controls missions that operate multiple satellites simultaneously, such as the multistatic SAR system [19–21]. As the ground-station contact period becomes longer, the orbit or attitude control parameter error due to propagation increases. This error significantly degrades the orbit and attitude control performance of the multi-satellite system [21]. In addition, when the ground station controls multiple satellites, the required performance or the number of ground stations increases, and this increases the mission cost and the workload of the ground station [19,20]. Many studies have been conducted on autonomous formation flying for efficient mission performance of multiple satellites, and it was applied to TechSat-21, DART, and VISORS missions [19,21,22]. However, almost all SAR missions do not use autonomous orbit and attitude control algorithms and proceed according to schedule files received from ground stations [21,23].

This study has three main contributions. First, a multistatic SAR formation-flying system that enables continuous SAR imaging like stripmap mode for very-high-resolution SAR images using SAR microsatellites with a manufacturable and reasonable specification is presented. To obtain a very-high-resolution SAR image, the signal received from the target must have sufficient Doppler bandwidth. The multistatic SAR system presented in this paper increases the Doppler bandwidth through the formation flying of multiple SAR satellites, unlike the existing monostatic SAR satellites using spotlight mode. This multistatic SAR system enables continuous very-high-resolution SAR imaging because no additional maneuvers are required to increase the Doppler bandwidth.

The second contribution is developing and verifying the autonomous relative orbit and attitude control algorithms for multistatic SAR system operation. Controlling the orbit and attitude of a multistatic SAR system by a ground station entails the degradation of control performance and operational limitations due to orbit estimation errors. Because the autonomous orbit control algorithm presented in this paper uses the relative orbital elements obtained using GPS data, the orbital control period can be set according to the allowable relative position error. The autonomous attitude control algorithm allows the satellite to independently determine the SAR imaging mode according to the right ascension of the descending node (RADN) it passes and to accurately calculate the attitude for target pointing.

The final contribution is to analyze the effect of navigation and attitude errors on SAR images through multistatic SAR imaging simulation and to obtain navigation and attitude requirements for very-high-resolution multistatic SAR images. The performance of SAR imaging using physically separated multiple satellites is degraded due to the received signal phase error caused by absolute and relative navigation errors. A phase correction algorithm is proposed through analysis of the properties of this phase error. Additionally, by analyzing the effects of various factors of navigation and attitude errors on multistatic SAR imaging, the requirements related to navigation and attitude for very-high-resolution multistatic SAR imaging were derived.

Section 2 presents the preliminary design of a multistatic SAR formation system for very-high-resolution stripmap imaging (VHRSI). In Section 3, relative orbit control algorithms for maintenance of multistatic SAR formation are designed and verified by simulation. Section 4 presents autonomous attitude control strategies and algorithms for each satellite for VHRSI. Section 5 verifies the performance of VHRSI through multistatic SAR imaging simulation reflecting the navigation and attitude errors, and relative orbit and attitude control requirements are derived through the analysis of multistatic SAR image quality according to navigation and attitude error.

2. Preliminary Design of a Multistatic SAR Formation System for VHRSI

2.1. Top-Level Requirements of Multistatic SAR System

This study aims to develop a multistatic SAR system capable of imaging very-high-resolution SAR images in stripmap mode using SAR microsatellites with reasonable specifications. Here, very-high-resolution means a spatial resolution of 0.5–1 m [24,25]. Although the required resolution differs depending on the application field of the SAR image, the demand for submeter-level high-resolution images has been increasing recently. In particular, the national defense field requires very-high-resolution images to detect and identify essential targets.

According to the Civil National Image Interpretability Rating Scale data in Table 1 [26], which lists detectable and identifiable targets for the resolution category, a level 5 image with a resolution of 0.75–1.2 m is required to detect or identify key targets. Therefore, the top-level requirements of the multistatic SAR system for VHRSI are to perform continuous SAR imaging, such as stripmap mode, and provide very-high spatial resolution.

Table 1. Civil National Image Interpretability Rating Scale category of radar images [26].

| Category | Specification |
|-------------------------|--|
| Level 3 (2.5~4.5 m) | <ul style="list-style-type: none"> - Detect individual houses in residential neighborhoods - Identify inland waterways navigable by barges |
| Level 4 (1.2~2.5 m) | <ul style="list-style-type: none"> - Detect basketball court, tennis court in urban areas - Identify buildings and large ships |
| Level 5 (0.75~1.2 m) | <ul style="list-style-type: none"> - Identify individual tracks, rail pairs, control towers - Identify tents (larger than two person) at established areas - Identify individual rail cars by type (e.g., gondola, flat, box) - Detect large animals (e.g., elephants, giraffes) in grasslands |

2.2. Methodology for Improving the Resolution of a SAR Image

Figure 1 shows the geometry of SAR images based on radar theory. The SAR image is in two dimensions (2D). The spatial resolution of the SAR image is expressed as the range resolution (δR_r) as presented in Equation (1) and the azimuth resolution (δR_a) as shown in Equation (2) [27]. The equations for the range and azimuth resolutions are expressed as follows:

$$\delta R_r = \frac{c}{2BW_p} \frac{1}{\sin \theta_i} \quad (1)$$

$$\delta R_a = \frac{\lambda R}{2L_{SA}} = \frac{D_a}{2} \quad (2)$$

where c is the propagation speed of a signal, BW_p is the pulse bandwidth, θ_i is the incidence angle, which is the angle between the radar beam and the normal to Earth's surface, λ is the wavelength of the signal, R is the slant range between the satellite and the target, L_{SA} is the synthetic aperture length, which is the moving distance of the satellite when the antenna beam illuminates the target, and D_a is the antenna diameter in the satellite velocity (along-track) direction. However, the spatial resolutions obtained by Equations (1) and (2) are the maximum theoretical values [28]. In practice, the spatial resolution is degraded by various factors, such as phase error of the received signal and instability of the radar signal [27,28].

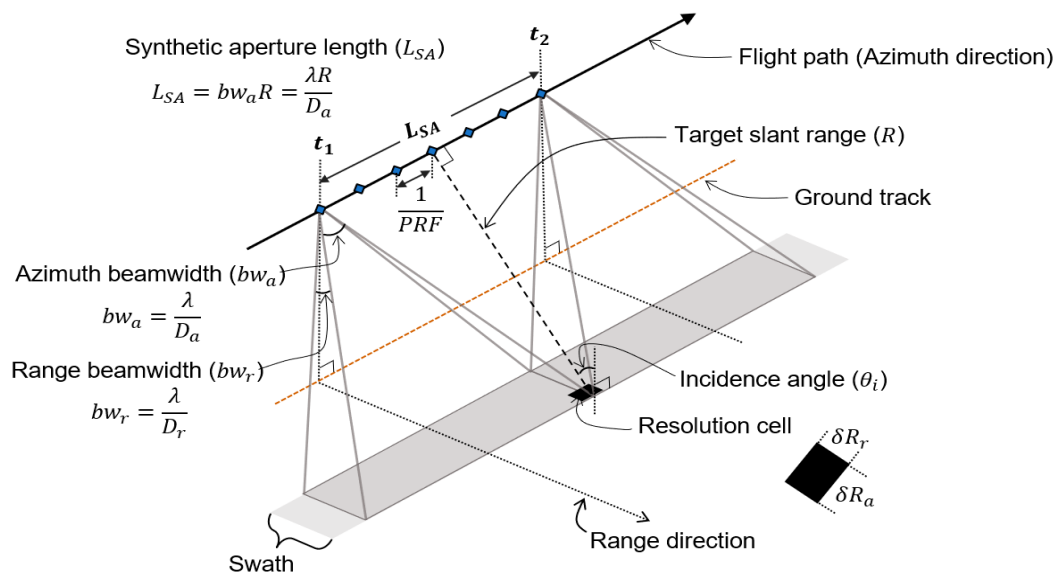


Figure 1. Geometry of SAR imaging.

Methods for improving the spatial resolution are derived using Equations (1) and (2). δR_r can be enhanced by expanding the pulse bandwidth (BW_p) or increasing the incidence angle (θ_i). Here, BW_p is limited by the performance of the pulse generator, and θ_i is determined by the microwave scattering characteristics of the target, transmission power, and sensitivity of the receiver. Therefore, the range resolution can be improved through the performance upgrade of the SAR subsystems. Azimuth resolution can be enhanced by increasing the synthetic aperture length (L_{SA}), i.e., reducing D_a or applying spotlight mode. However, the method of reducing the size of the SAR antenna is limited by the rapid increase in the required transmission power, and the spotlight mode has restrictions such as a narrow observation area and discontinuous imaging.

In this study, the multistatic SAR concept is applied as a method of increasing L_{SA} for δR_a enhancement, as shown in Figure 2 [1]. The multistatic SAR system for VHRSI is designed as an along-track formation consisting of a chief satellite that transmits and receives signals and two deputy satellites that receive only and make all antennas point to the same target. Consequently, L_{SA} is increased, and δR_a is improved by synthesizing signals of various bandwidths received by each satellite.

2.3. Formation Design of Multistatic SAR Satellites

For a very-high-resolution SAR image, the range and azimuth resolutions must be less than 1 m. SAR microsatellites using an X-band microwave can achieve a sub-meter class range resolution by setting an appropriate BW_p . Conversely, obtaining the synthetic aperture length for sub-meter-class azimuth resolution is difficult due to the high hardware load in the single-channel stripmap mode. Therefore, we try to obtain a suitable synthetic aperture length using the multistatic SAR concept.

The specifications of the multistatic SAR microsatellite are listed in Table 2. Most SAR microsatellite specifications for VHRSI are similar to ICEYE-2 [29]. However, the antenna size is set to 2.2 m to obtain a sufficient synthetic aperture length. To get multistatic SAR formation for VHRSI using satellite specifications, as shown in Table 2, the optimal value of the total synthetic aperture length of the multistatic SAR system ($L_{SA,MS}$) should be calculated.

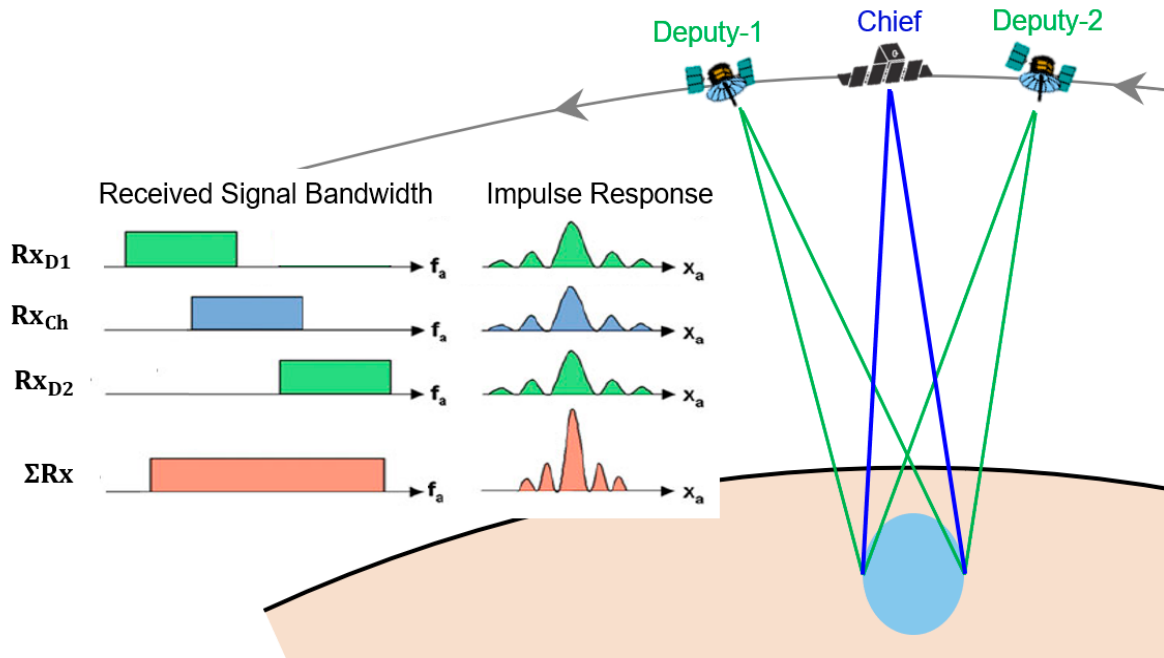


Figure 2. Multistatic SAR concept for VHRSI. Three satellites receive signals of different bandwidths due to the Doppler frequency gap. The synthesis of all received signals sharpens the impulse response, implying an improvement in azimuth resolution.

Table 2. Specification of the multistatic SAR microsatellite [29].

| Contents | Specification |
|----------------------------------|-------------------|
| Altitude | 570 km |
| Antenna size | 2.2 m × 0.5 m |
| Carrier frequency | X-band (9.65 GHz) |
| Incidence angle | 25°~35° |
| Pulse bandwidth (BW_p) | 400 MHz |
| Pulse repetition frequency (PRF) | 11 kHz |
| Aperture time | 1.4 s |

According to Equation (2), the theoretical $D_{a,\delta R_a=1}$, antenna diameter of the azimuth direction allowing the azimuth resolution to be 1 m, is 2 m. The theoretical $L_{SA,\delta R_a=1}$, synthetic aperture length when D_a is 2 m, was calculated to be 10.2 km, using Equation (3).

$$L_{SA} = \frac{c R}{f_C D_a}, \quad (3)$$

where f_C is the carrier frequency. However, the azimuth resolution of SAR microsatellites using a slot antenna is approximately 50% degraded [29,30]. Therefore, $L_{SA,MS}$ should be designed greater than twice the theoretical $L_{SA,\delta R_a=1}$ as shown in Equation (4):

$$L_{SA,MS} \geq 2 L_{SA,\delta R_a=1}. \quad (4)$$

Figure 3 represents the synthetic aperture length of the multistatic SAR system for VHRSSI ($L_{SA,MS}$) consisting of three SAR microsatellites with the specifications presented in Table 2. The three ellipses mean the synthetic aperture length of each SAR microsatellite with an antenna length of 2.2 m ($L_{SA,D_a}=2.2$), and each $L_{SA,D_a}=2.2$ is 9.3 km. To satisfy Equation (4), $L_{SA,MS}$ must be set to 20.4 km or more. To meet this requirement, the baseline between satellites is set to 6 km as shown in Figure 3. Consequently, $L_{SA,MS}$ becomes 21.3 km, and the synthetic aperture length of each satellite overlaps by 3.3 km.

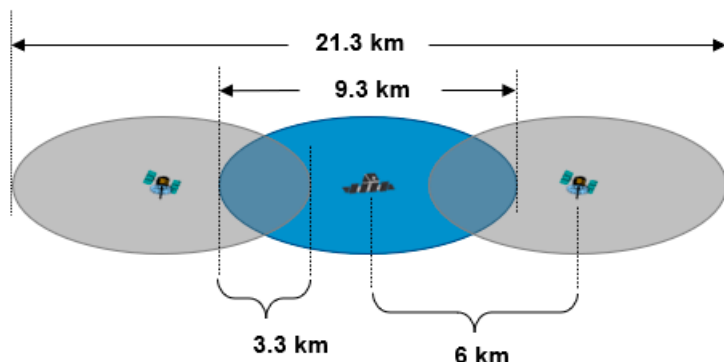


Figure 3. Synthetic aperture length of a multistatic SAR system ($L_{SA,MS}$). The baseline between each satellite is 6 km, and $L_{SA,MS}$ is 21.3 km. The synthetic aperture length of each satellite is equal to 9.3 km, and the overlap is 3.3 km.

3. Design of the Relative-Orbit-Control Algorithm for Multistatic SAR Formation-Flying

To obtain VHRSSI, the multistatic SAR formation obtained in Section 2 must be maintained continuously. However, because each satellite is affected by different perturbations, the relative distances of the multistatic SAR satellites change. Therefore, the relative orbit must be controlled to maintain the relative distance between satellites within the proper boundary [21].

Requirements of the relative orbit control algorithm to maintain the multistatic SAR formation are as follows.

- (1) The relative distance (baseline) should be maintained at 6000 ± 100 m for the along-track direction. Here, the error criterion of 100 m is set as half of the ground-station based relative orbital control error of the multistatic SAR mission of TerraSAR-X and TanDEM-X [31].
- (2) The magnitude of the thrust used for relative orbit control shall not exceed the performance of the thruster suitable for microsatellites.
- (3) The total Δv used during the lifetime of the satellite shall not exceed the total fuel of the thrusters.

In this section, a relative orbit control algorithm that reflects the performances of the COTS thruster suitable for the SAR microsatellite as constraints is designed. Subsequently, the verification of the relative orbit control algorithm is performed through numerical simulation.

3.1. Relative Orbit Control Algorithm for the Along-Track Formation Maintenance

The along-track formation maintenance means keeping the relative argument of latitude (δu) roughly constant, given that the orbital shape of each satellite is similar. The formation maintenance algorithm of multistatic SAR satellites allows for maintaining the relative position by using a method to keep the mean relative orbital elements of the deputy satellite with respect to the chief satellite near the desired value [21]. Figure 4 is a flowchart of the relative orbit control algorithm for formation flying of a multistatic SAR system, and it will be explained in detail in the subsection.

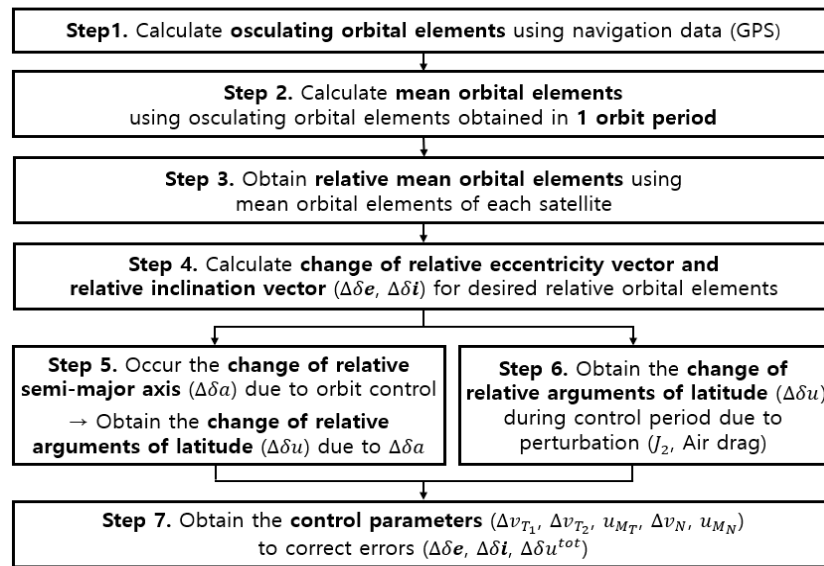


Figure 4. Flowchart of the relative orbit control algorithm for formation maintenance using relative orbital elements.

3.1.1. Calculations of the Mean Relative Orbital Elements (Steps 1, 2, and 3 in Figure 4)

The process of obtaining mean relative orbital elements starts with calculating the absolute orbital elements of each satellite. Orbital elements can be obtained on board through the orbit determination process using GPS data. The vector of the absolute orbital elements (α) of the chief satellite, which is the basis for formation flying, in the Earth-Centered Inertial (ECI) frame is as follows [21,32]:

$$\alpha = \begin{bmatrix} a \\ u \\ e_x \\ e_y \\ i \\ \Omega \end{bmatrix} = \begin{bmatrix} a \\ \omega + M \\ e \cos \omega \\ e \sin \omega \\ i \\ \Omega \end{bmatrix}, \quad (5)$$

where a , e , i , ω , Ω , and M are the classical Keplerian orbital elements; here, a is the semimajor axis, e is the eccentricity, ω is the argument of perigee, M is mean anomaly, i is the inclination, and Ω is the right ascension of the ascending node (RAAN). Moreover, α is a vector of orbital elements using the eccentricity vector $\mathbf{e} = (e_x, e_y)^T$ and the mean argument of latitude u . The mean argument of latitude can solve singularities that occur in near-circular orbit.

The relative motion of the deputy satellite with respect to the chief satellite can be expressed through the relative orbital elements ($\delta\alpha$) vector as follows [21,32]

$$\delta\alpha = \begin{bmatrix} \delta a \\ \delta \lambda \\ \delta e_x \\ \delta e_y \\ \delta i_x \\ \delta i_y \end{bmatrix} = \begin{bmatrix} \delta a \\ \delta \lambda \\ \delta e \cos \varphi \\ \delta e \sin \varphi \\ \delta i \cos \theta \\ \delta i \sin \theta \end{bmatrix} = \begin{bmatrix} (a_d - a)/a \\ (u_d - u) + (\Omega_d - \Omega) \cos i \\ e_{x_d} - e_x \\ e_{y_d} - e_y \\ i_d - i \\ (\Omega_d - \Omega) \sin i \end{bmatrix}, \quad (6)$$

where, the subscript d denotes the deputy satellites; δa is the relative semimajor axis, which is the difference in the semimajor axis normalized to the semimajor axis of the chief satellite for setting the dimensionless variable; $\delta\lambda$ is the relative mean along-track offset angle; $\begin{pmatrix} \delta e_x \\ \delta e_y \end{pmatrix} = \delta e \begin{pmatrix} \cos \varphi \\ \sin \varphi \end{pmatrix}$ and $\begin{pmatrix} \delta i_x \\ \delta i_y \end{pmatrix} = \delta i \begin{pmatrix} \cos \theta \\ \sin \theta \end{pmatrix}$ are the two-dimensional cartesian elements

and polar coordinates elements of the relative eccentricity vector (δe) and the relative inclination vector (δi), respectively; δe and δi are used to express in-plane and out-of-plane relative motion, respectively; φ and ϑ are the phases of δe and δi , respectively, which represent the angular location of the relative perigee and relative ascending node [21,32].

3.1.2. Calculation of the Control Value of Relative Eccentricity and Inclination ($\Delta\delta e$ and $\Delta\delta i$) for Desired Relative Orbit Motion (Step 4 in Figure 4)

The equations of the deputy satellite's relative motion with respect to the chief satellite in near-circular orbit can be linearized, and to express this visually, it can be expressed in the RTN frame (local orbital frame) as follows [21,32]:

$$\delta r(\delta \alpha(u_0), u) = \begin{pmatrix} \delta r_R \\ \delta r_T \\ \delta r_N \end{pmatrix} = a \begin{pmatrix} \delta a - \delta e \cos(u - \varphi) \\ \delta \lambda - 1.5\delta a(u - u_0) + 2\delta e \sin(u - \varphi) \\ \delta i \sin(u - \vartheta) \end{pmatrix}, \quad (7)$$

where the RTN frame is a local coordinate system with the position of the chief satellite as the origin. R, T, and N axes are parallel to the radial vector of the chief, the unit vector of N × R (velocity vector of the chief in the case of a circular orbit), and the angular momentum vector of the chief orbit, respectively. As relative orbital motion is expressed using relative orbital elements, perturbations such as J_2 and air drag can be conveniently reflected in the equation of relative motion. The relative orbital elements that reflect these perturbations when the mean argument of latitude of a chief is u can be expressed as follows [21,32]:

$$\delta \alpha(u) = \begin{bmatrix} \delta a \\ \delta \lambda - 10.5\gamma \sin(2i)\delta i_x(u - u_0) \\ \delta e \cos(\varphi + \varphi'(u - u_0)) \\ \delta e \sin(\varphi + \varphi'(u - u_0)) \\ \delta i_x \\ \delta i_y + 3\gamma \sin^2(i)\delta i_x(u - u_0) \end{bmatrix}_{J_2} + \begin{bmatrix} -\Delta B\rho a(u - u_0) \\ 3\Delta B\rho a(u - u_0)^2/4 \\ 0 \\ 0 \\ 0 \\ 0 \end{bmatrix}_{air\ drag} \quad (8)$$

where, the first and second terms are relative orbital elements that reflect J_2 perturbations and differential air drag, respectively; $\gamma = J_2 R_e^2 / 2a^2$ is the J_2 factor; R_e is the Earth's mean equatorial radius; $\varphi' = d\varphi/dt = 3\gamma(5\cos^2(i) - 1)/2$ is the derivative of the relative perigee; ΔB is the difference in ballistic coefficients $B = AC_D/m$ of each satellite, A is the cross-section area, C_D is the drag coefficient, m is the mass of the satellite, and ρ is the atmospheric density. The substitution of the relative orbital elements of Equation (8) into Equation (7) can provide a first-order approximation solution of the equation of relative motion that reflects J_2 and differential air drag.

The relative eccentricity vector δe and the relative inclination vector δi determine the secular variations of in-plane and out-of-plane relative orbit, respectively. Therefore, to maintain the relative orbit within the desired error limit, δe and δi must be controlled within the calculated boundary.

Figure 5 represents the change of δe and the δi by J_2 obtained through Equation (8), where the superscript *max* denotes the maximum allowable error, *nom* denotes the desired relative orbital elements, *man* denotes the value to be adjusted through relative orbit control, and *start* denotes the maximum start point of the relative orbit control. If $\varphi' < 0$ and $\delta i_x > 0$, δe rotates clockwise and δi increases along the y-axis due to effect of J_2 according to Equation (8). The change in δe and δi is proportional to time. Therefore, it is possible to calculate the phase change of δe that occurs during one orbit control period. Here, δe^{man} is set such that the middle value of the phase change is located at δe^{nom} , as shown in Equation (9) [21,32].

$$\delta e^{man} = \mathbf{R}_z(\delta\varphi)\delta e^{nom} = \begin{pmatrix} \delta e_x^{nom} \cos(\delta\varphi) - \delta e_y^{nom} \sin(\delta\varphi) \\ \delta e_x^{nom} \sin(\delta\varphi) + \delta e_y^{nom} \cos(\delta\varphi) \end{pmatrix}, \quad (9)$$

where $\delta\varphi \approx \text{sign}\varphi' \arcsin(|\delta e^{max}|/|\delta e^{nom}|)$ denotes the maximum allowable deviation of the relative perigee from φ^{nom} , and R_z is the rotation matrix for the z-axis.

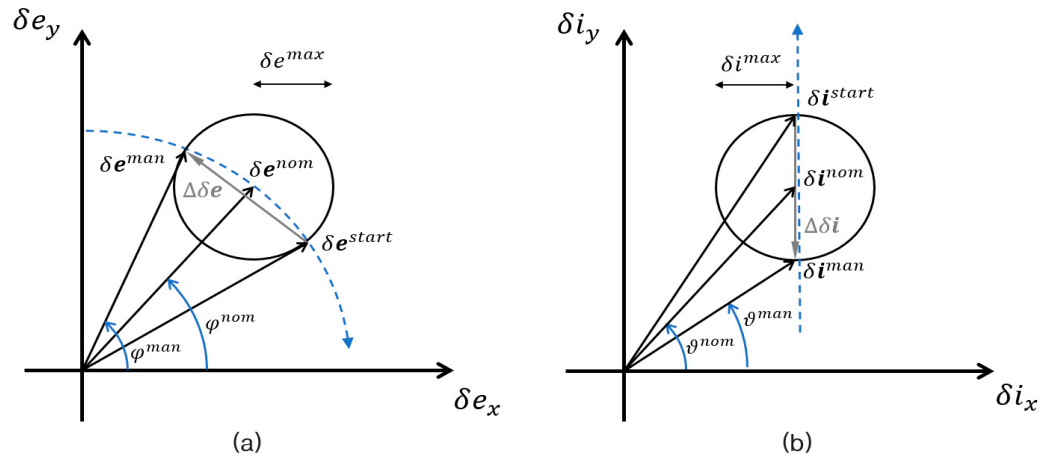


Figure 5. Relative orbit control concept for the relative eccentricity vector δe (a) and relative inclination vector δi (b) changed by the secular J_2 effect.

The value of δi^{man} is also set such that the center value of the variation of δi is located at δi^{nom} , as shown in Equation (10) [21,32].

$$\delta i^{man} = \left(\begin{array}{c} \delta i_x^{nom} \\ \delta i_y^{nom} - \text{sign}(\delta i_x) \delta i^{max} \end{array} \right) \quad (10)$$

Therefore, formulas used to determine $\Delta\delta e$ and $\Delta\delta i$ through relative orbit control are $\delta e^{man} - \delta e$ and $\delta i^{man} - \delta i$, respectively.

3.1.3. Calculations of the Control Value of the Relative Semimajor Axis ($\Delta\delta a$) to Maintain the Desired Relative Mean Argument of Latitude δu (Steps 5 and 6 in Figure 4)

The relative semimajor axis δa is controlled to correct the error of the relative mean argument of latitude δu , which is generated by various factors during the in-plane relative orbit control. During the period between each in-plane relative orbit control, δu is changed by J_2 and the differential air drag, which are determined using Equations (6) and (8). Furthermore, because in-plane relative orbit control consists of two impulse maneuvers, δu is changed between two impulses by the value of δa required for $\Delta\delta e$ correction. The value of δa^{man} , which must be adjusted through relative in-plane orbit control, is set such that the middle value of the total change in δu that occurs during one cycle of in-plane relative orbit control becomes the desired relative mean argument of latitude δu^{nom} , as shown in Equation (11) [21].

$$\delta a^{man} \approx -\frac{\pi}{2n\Delta t - \pi} \left[3\delta e^{max} + \delta a - \frac{4}{3\pi} (\delta u - \delta u^{nom} + \delta u_{J_2} + \delta u_D) \right] \quad (11)$$

where δa^{man} is the maneuver point of the relative semimajor axis that causes δu to oscillate about δu^{nom} ; n is the mean motion of the chief orbit $\sqrt{\mu/a^3}$, Δt is the maneuver cycle, δu_{J_2} and δu_D are the variation of the relative mean argument of latitude that arises from J_2 and differential air drag (D), respectively. Therefore, $\Delta\delta$ through relative orbit control is $\delta a^{man} - \delta a$.

3.1.4. Calculations of Control Parameters $\Delta v_T, u_{M_T}, \Delta v_N, u_{M_N}$ (Step 6 in Figure 4)

In a near-circular non-equatorial orbit situation, Δv for controlling the relative orbit is obtained through the Gauss' variation equation that linearizes the variation of the relative

orbital elements according to the change in velocity (δv_R , δv_T , δv_N) in the RTN frame [21,32]. Here, δv_R , δv_T , and δv_N are the components of Δv with respect to the RTN frame.

$$\begin{bmatrix} a\Delta\delta a \\ a\Delta\delta\lambda \\ a\Delta\delta e_x \\ a\Delta\delta e_y \\ a\Delta\delta i_x \\ a\Delta\delta i_y \end{bmatrix} \approx \begin{bmatrix} 2\delta v_T/n \\ -2\delta v_R/n - 3(u - u_M)\delta v_T/n \\ \delta v_R \sin u_M/n + 2\delta v_T \cos u_M/n \\ -\delta v_R \cos u_M/n + 2\delta v_T \sin u_M/n \\ \delta v_N \cos u_M/n \\ \delta v_N \sin u_M/n \end{bmatrix} \quad (12)$$

As in Equation (12), the change in the relative orbital elements induced by the variation of the velocity is decoupled as in-plane and out-of-plane maneuvers in the RTN frame. In-plane relative orbit control parameters are calculated by the inversion of the four equations at the top within Equation (12). Particularly, when the constraints of minimizing the thrust cost and maneuvering with two impulses are applied, the in-plane relative orbit control parameters δv_{T_1} , δv_{T_2} , δv_{R_1} , δv_{R_2} , u_{M_1} , and u_{M_2} are obtained as shown in Equation (13) [21]. Subscripts 1 and 2 denote the first and second in-plane maneuvers, respectively.

$$\begin{bmatrix} \delta v_{T_1} \\ \delta v_{R_1} \\ \delta v_{T_2} \\ \delta v_{R_2} \end{bmatrix} = \frac{na}{4} \begin{bmatrix} \Delta\delta a + ||\Delta\delta e|| \\ 0 \\ \Delta\delta a - ||\Delta\delta e|| \\ 0 \end{bmatrix}, \begin{bmatrix} u_{M_1} \\ u_{M_2} \end{bmatrix} = \begin{bmatrix} \arctan\left(\frac{\delta e_y^{man} - \delta e_y}{\delta e_x^{man} - \delta e_x}\right) \\ u_{M_1} + \pi \end{bmatrix}, \quad (13)$$

where, $\Delta\delta a = \delta a^{man} - \delta a$, $\Delta\delta e = \delta e^{man} - \delta e$, and u_{M_1} and u_{M_2} are the mean arguments of latitudes at the first and second impulses of the in-plane maneuver, respectively.

In the condition of a single impulse maneuver, the out-of-plane relative orbit control parameters δv_n and u_{M_n} are obtained as in Equation (14)

$$\delta v_n = na||\Delta\delta i||, u_{M_n} = \arctan\left[\left(\delta i_y^{man} - \delta i_y\right)/\left(\delta i_x^{man} - \delta i_x\right)\right], \quad (14)$$

where $\Delta\delta i = \delta i^{man} - \delta i$, and u_{M_n} is the mean argument of latitude at the impulse of the out-of-plane maneuver.

3.2. Numerical Simulations of Relative Orbit Control for the Along-Track Formation Maintenance

In this section, the relative orbit control algorithm to maintain the multistatic SAR formation for VHRSI designed in Section 2 is verified using numerical simulations. This verification process demonstrates that the analytically designed orbit control algorithm applying linearization and approximation will work in the real orbital environment with various orbital perturbations. The reference orbit of the chief satellite is set as a sun-synchronous near-circular orbit with an altitude of 570 km, and the relative orbit of the deputy satellite with respect to the chief reflects the along-track formation of 7.5 km baseline, as shown in Table 3. Here, the 7.5 km baseline reflects the final designed multistatic SAR formation for VHRSI presented in Section 5 by analysis of multistatic SAR images. In fact, the relative orbit control simulation was performed first at the baseline of 6 km, and after the multi-static SAR image analysis, the relative orbit control simulation was performed again at the baseline of 7.5 km. Because the results of the two relative orbit control simulations were almost identical, the final result of 7.5 km is reflected to avoid redundancy in the text.

The simulation conditions of the dynamic model and control parameters are shown in Table 4. The initial conditions of chief and deputy satellites for simulation are the states presented in Table 3. The epoch time of the simulation was 00:00:00 on 1 January 2020, and the simulation duration was 5 days. It is assumed that the shape and all specifications, including the data in Table 2, of the chief and deputy satellites are similar, but the air drag area of each satellite is set differently to confirm the performance of the relative orbit control. It is assumed that the shape and specifications of the chief and deputy satellites, including the data in Table 2, are identical. However, to confirm the performance of the relative orbit control, the air drag

area of each satellite is set differently. This air drag area setup may be reasonable because the multistatic SAR system can be composed of chief and deputy satellites with different shapes. The initial relative position and velocity errors of the deputy satellite are set as Gaussian random errors of 50 m and 0.5 m/s for the nominal values. Because the relative orbit control results of lead and trail deputies are similar except for the opposite relative positions in the along-track direction, only trail deputy results are analyzed.

Table 3. Orbital elements of the chief satellite and relative orbital elements of the deputy satellite.

| Orbital Elements of the Chief Satellite | | Relative Orbital Elements of the Deputy Satellite | |
|---|---------------|---|---------|
| a | 6378 + 570 km | $a\delta a^{nom}$ | 0 m |
| u | 0° | $a\delta\lambda^{nom}$ | -7500 m |
| e_x | 0.0001 | $a\delta e_x^{nom}$ | 0 m |
| e_y | 0 | $a\delta e_y^{nom}$ | 0 m |
| i | 98.19° | $a\delta i_x^{nom}$ | 0 m |
| Ω | 189.89° | $a\delta i_y^{nom}$ | 0 m |

Table 4. Simulation conditions of the dynamic model and orbit control parameters.

| | Contents | Specifications |
|-------------------------------|------------------------------------|---|
| Dynamic model | Gravity model | JGM-3 60 by 60 |
| | Third body perturbation | Sun, Moon, Planets (DE405) |
| | Air drag model | MSISE00 |
| | Solar radiation pressure | Conical spherical model |
| Parameters for orbit controls | Drag area | 1.0 m ² (chief)/1.5 m ² (deputy) |
| | Mass | 100 kg |
| | Orbit determination error | 2 m, 0.02 m/s (1σ) |
| | Relative orbit determination error | 0.1 m, 0.001 m/s (1σ) |
| | Δv direction error | 1° (3σ) |
| | control interval | In-plane: 5 orbit periods Out-of-plane: $a \delta\mathbf{i} \geq 5$ m |

Figure 6a,b show the relative position and relative position error of the trail deputy satellite, respectively, with respect to the designed nominal relative position in the RTN frame over elapsed time. The simulation of relative orbit control reflecting the conditions of Tables 3 and 4 satisfied the requirements for relative distance (<100 m, 3σ). Owing to the initial relative position and velocity error, a relative position error occurred at approximately 120 m and 600 m in the radial and along-track directions, respectively. Through five in-plane orbit controls (approximately 42 h), the relative position error of the R-axis and T-axis converges within the requirement, and then the relative distance error is maintained consistently within 45 m (3σ). The relative position error in the N-axis direction, which is gradually increased by geopotential perturbation, is maintained within approximately 10 m (3σ) through out-of-plane relative orbital control.

Figure 7 denotes the changes in the eccentricity vector on the vector plane (a) and the eccentricity vector element over elapsed time (b) due to relative orbit control. Owing to the initial relative position and velocity errors of the deputy satellite, the error of the relative eccentricity vector to be corrected occurred more than 150 m in the y-axis direction. The relative distance error in the along-track direction was twice the magnitude of the relative eccentricity vector. Therefore, the magnitude of the relative eccentricity vector was maintained within 50 m to meet the relative distance requirement of 100 m. Through in-plane relative orbit control, the relative eccentricity vector converged within 50 m and was continuously maintained within 20 m.

Figure 8 shows the changes in the relative semimajor axis (a), the relative mean argument of longitude (b), and relative inclination vector elements (c) over elapsed time due to relative orbit control. The relative semimajor axis oscillates for 20 m by short periodic

geopotential perturbation. Additionally, for in-plane relative orbit control, the center of the amplitude of the relative semimajor axis is controlled based on zero. The relative mean argument of longitude is maintained after converging at the designed relative position of the deputy satellite, -7500 m, through the control of the relative semimajor axis. The relative inclination increased by geopotential perturbations is maintained within 10 m through out-of-plane relative orbit control.

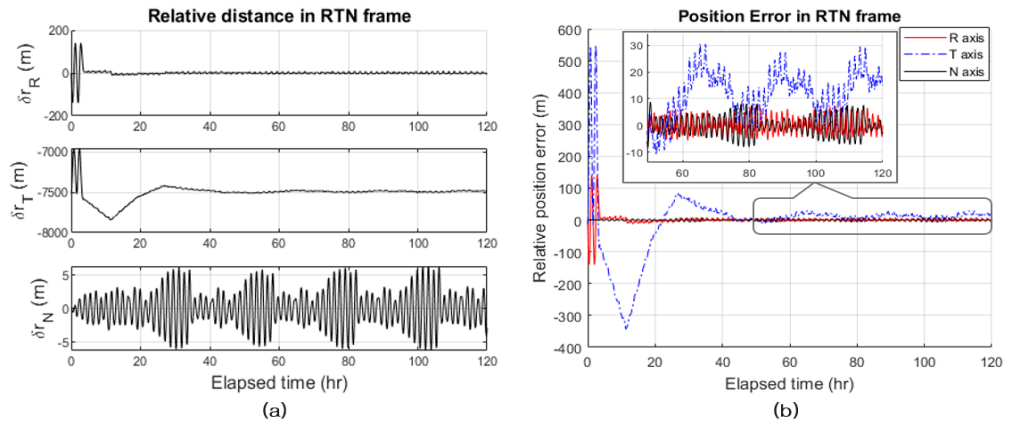


Figure 6. Simulation results of the relative orbit control algorithm. The relative position of the trail deputy satellite (a), and the position error with respect to the nominal relative position (b) in the RTN frame over elapsed time.

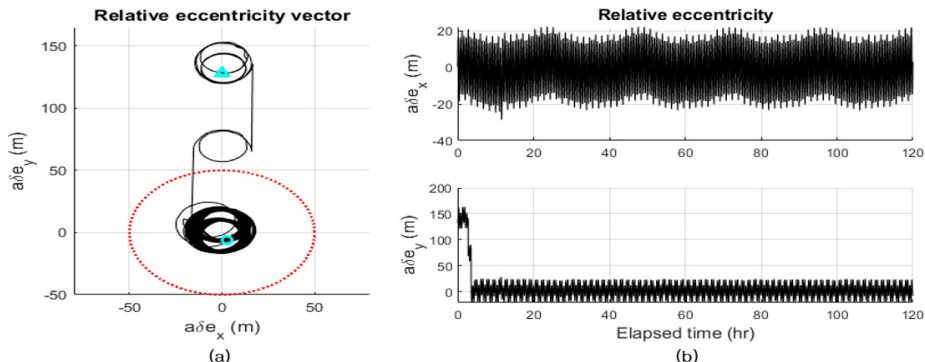


Figure 7. Simulation results of the relative orbit control algorithm. Relative eccentricity vector on the vector plane (a), and relative eccentricity vector elements over elapsed time (b). The triangle and circle markers in (a) are the initial and final positions of the relative eccentricity vector, respectively. The red dotted line is the maximum error boundary for satisfying the relative distance requirement.

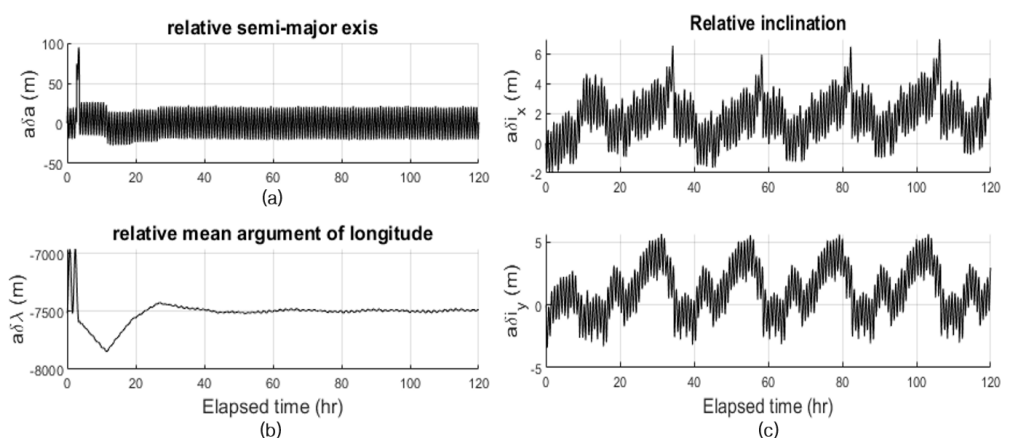


Figure 8. Simulation results of the relative orbit control algorithm. Relative semimajor axis (a), relative mean argument of longitude (b), and relative inclination vector elements (c) over elapsed time.

Figure 9 denotes the control profile of the relative orbit control (a) and the accumulated Δv used for relative orbit control (b). To correct the initial relative position error of the deputy satellite, Δv of 75 mm/s was used in the first in-plane maneuver. After the formation was stable, a thrust of approximately 2 mm/s was used for each in-plane maneuver. Out-of-plane maneuvers were performed once every 20 orbital cycles, and the value of Δv used in each maneuver was approximately 7 mm/s. The average Δv per day used for relative orbit control was approximately 11 mm/s, which is within the performance range of the Hall effect ion thruster.

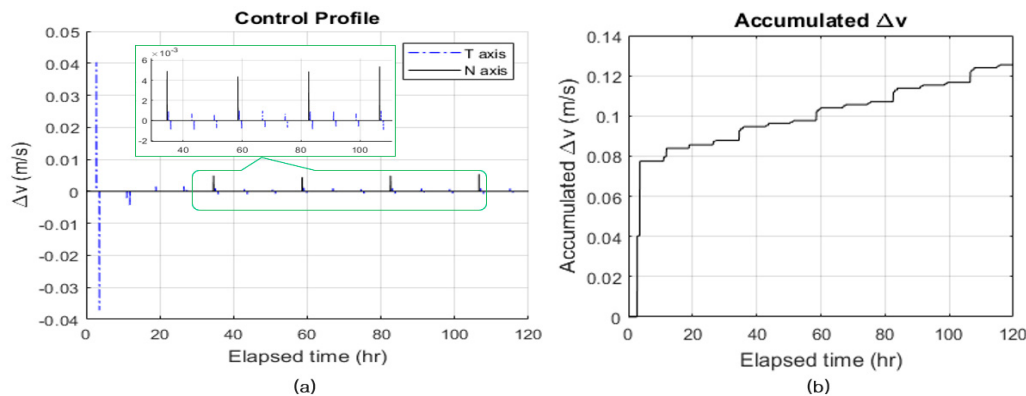


Figure 9. Simulation results of the relative orbit control algorithm. Thrust profile used for relative orbit control (a) and accumulated Δv (b) over elapsed time. The blue dotted line in (a) is the in-plane control thrust and the black solid line is the out-of-plane control thrust.

3.3. Performance Analysis of Thrusters for Orbit Control

In microsatellites, cold gas or ion thrusters are used for orbit control, considering the mounting space constraint and the thrusters' safe operation [33]. The cold gas thruster is relatively fine in terms of cost and thrust magnitude, and the ion thruster is superior in specific impulse (I_{sp}), indicating the efficiency of the thruster. Therefore, a thruster suitable for the mission is selected by considering the required thrust magnitude, the total impulse required during its lifetime, the weight and volume constraints to be installed on the satellite, etc. [33]. The SAR microsatellite applied in this research is assumed to have a mass of less than 100 kg and a lifetime of 5 years or more. Because the SAR microsatellite must perform orbit control at a daily level for more than five years, it is appropriate to apply the ion thruster. In addition, considering the satellite mass of 100 kg, it is reasonable to apply the Hall effect ion thruster with the highest thrust among ion thrusters. Hall effect ion thrusters have considerable heritage, including Starlink of SpaceX, and they have a thrust range of 1~60 mN and a specific impulse range of 800~1950 s [33]. The BHT-200 thruster installed on the TacSat-2 and FalconSat-5/6 has a thrust of 13 mN, a specific impulse of 1390 s, and a total impulse of 13,000 Ns per kg of the propellant [33]. If a SAR microsatellite of 100 kg is equipped with a BHT-200 loaded with 5 kg of fuel, the total Δv available for five years of a lifetime is 650 m/s. This makes it possible to use a Δv of 350 mm/s per day on average.

As shown in the above simulation results, it was confirmed that the relative orbit control algorithm keeps the relative orbital elements within the bounds of requirement. The relative mean argument of longitude, the relative semimajor axis, and the relative eccentricity vector were controlled by in-plane maneuvers, and the relative inclination vector was controlled through out-of-plane maneuvers. Under the conditions reflecting the navigation errors and various perturbations, the relative distance error was maintained within 45 m, which satisfies the requirements of multistatic SAR formation for VHRSI.

4. Autonomous Attitude Control of Multistatic SAR Satellites for VHRSI

To obtain VHRSI, SAR antennas of three satellites must be aimed at the same ground target while performing SAR imaging. This section describes the development and verifica-

tion of an autonomous attitude control algorithm, applying the concept of the optimized RADN sectors for a multistatic SAR satellite. The requirements of the autonomous attitude control algorithm of the multistatic SAR system are as follows [33,34].

- (1) The antenna pointing error through attitude control must be within 0.01° (3σ).
- (2) The attitude stability during multistatic SAR imaging must be within $0.0007^\circ/\text{s}$ (3σ).
- (3) The attitude control for the multistatic SAR imaging must be completed at least 0.7 s before $\text{epoch}_{\text{SAR}}$. Because strip-map SAR imaging synthesizes received signals from the leading edge of the azimuth direction of the transmitted radar beam, SAR imaging starts before half the beam width from the target. Here, $\text{epoch}_{\text{SAR}}$ denotes a time point when the Doppler shift frequency of the chief satellite with respect to the ground target becomes zero.

4.1. Concept of the Optimal RADN (RADN_{op}) Sectors

General SAR satellites operate according to the mission profile received from the ground station [33]. In the case of these satellites, as the period from the connection with the ground station to the $\text{epoch}_{\text{SAR}}$ increases, the orbit estimation error increases, and the accuracy of the calculated attitude information degrades. In addition, simultaneous control of multiple satellites constituting a multistatic SAR system increases the workload of the ground station. To minimize the disadvantages of the ground-station control method, an autonomous attitude-control strategy using the RADN_{op} concept is applied, as shown in Figure 10. Figure 10a denotes the geometry of the satellite's orbit that passes through the ascending and left-side-looking RADN_{op} sector. Figure 10b represents the four RADN_{op} sectors on the equatorial plane that can perform the SAR imaging of the ground target located at $37.56413^\circ \text{ N}, 126.93470^\circ \text{ E}$, Science Hall of Yonsei University, Seoul. Here, RADN_{op} is the right ascension of the descending node of the satellite's orbit that enables imaging of a target at the desired incidence angle, and the red and blue arrows are RADN_{op} at the maximum incidence angle (35°) and minimum incidence angle (25°) conditions, respectively.

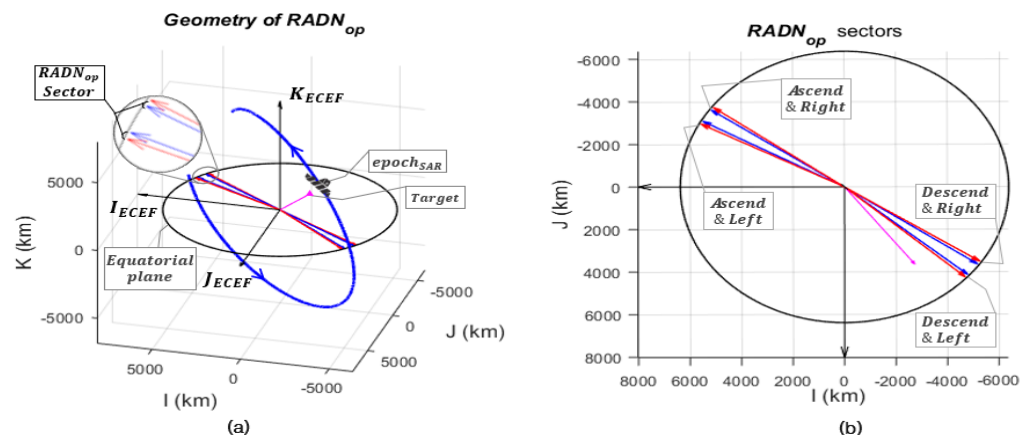


Figure 10. Geometry of RADN_{op} (a) and four RADN_{op} sectors in the equatorial plane (b) of the SAR microsatellite with respect to the ground target located at $37.56413^\circ \text{ N}, 126.93470^\circ \text{ E}$.

Using the RADN_{op} concept, the propagation time until $\text{epoch}_{\text{SAR}}$ does not exceed one orbital period; therefore, attitude information for multistatic SAR imaging can be calculated accurately. Additionally, the satellite can determine the SAR operation mode through the descending node position, thereby reducing the workload of the ground station. The length of the RADN_{op} sector is determined according to the incidence angle range and the latitude of the target. Four RADN_{op} sectors are set per target depending on the imaging situation, such as ascending or descending on orbit and left side or right side looking, as shown in Figure 10b. RADN_{op} is approximately calculated using a geometric method, and an

accurate $RADN_{op}$ is obtained through a numerical method, slightly adjusting the results of the geometric method.

4.1.1. Calculation of $RADN_{op}$ Using the Geometric Method

$RADN_{op}$ can be obtained using the geometrical relationship between the Earth's center, ground target, and satellite, as shown in Figure 11. Here, Earth and Satellite's orbits are assumed to be complete spheres and circular orbits, respectively. The data given to determine $RADN_{op}$ is the geodetic coordinates of the ground target, the semimajor axis a and inclination i of the orbital elements of the satellite, and the incidence angle of the radar beam θ_{inc} .

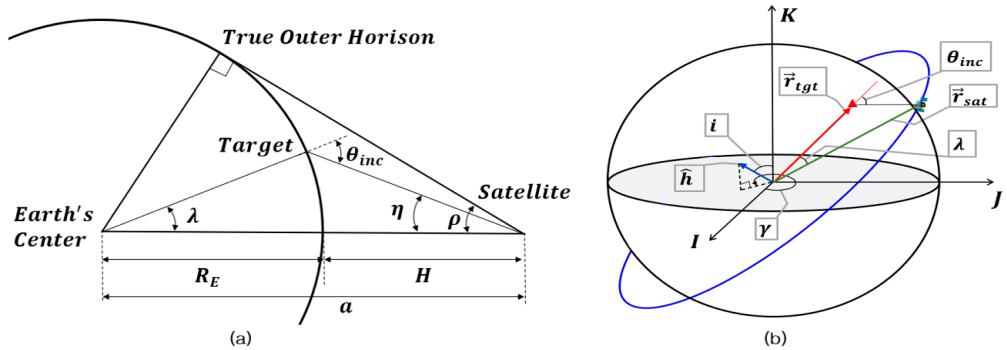


Figure 11. Geometric relationships between Earth's center, ground target, and satellite; 2D (a) and 3D (b).

Through the above conditions and the geometric relationship, as shown in Figure 11, the angle between the satellite and the target with respect to the Earth's center λ is calculated, as shown in Equations (15) and (16) [35].

$$\sin \eta = \frac{R_E}{a} \sin \theta_{inc}, \quad (15)$$

$$\lambda = \theta_{inc} - \eta, \quad (16)$$

where R_E is the radius of Earth, and η is the nadir angle to the target at the satellite position. As shown in Figure 11b, θ_{inc} is obtained at epoch_{SAR}, and at this moment, the target position vector with respect to the satellite and the velocity vector of the satellite are perpendicular. Therefore, the position vector of the satellite (\vec{r}_{sat}), the position vector of the target (\vec{r}_{tgt}), and the angular momentum unit vector of the circular orbit of the satellite (\hat{h}) exist in the same plane.

Considering spherical coordinates, \hat{h} in the ECI frame is expressed

$$\hat{h} = [\sin i \cos \gamma, \sin i \sin \gamma, \cos i], \quad (17)$$

where γ is the longitude of \hat{h} . To obtain γ , the dot product formula of \hat{h} and \vec{r}_{tgt} is used as follows:

$$\hat{h}_{ECEF} \cdot \vec{r}_{tgt} = r_{tgt} \sin(\pm \lambda), \quad (18)$$

where $+\lambda$ denotes the right-side-looking situation in which the target is located on the right with respect to the moving direction of the satellite. Conversely, $-\lambda$ denotes the left-side-looking situation. When $\vec{r}_{tgt} = [x_{tgt}, y_{tgt}, z_{tgt}]$, Equation (18) becomes a composite function form of a trigonometric equation, as shown in Equation (19).

$$\sqrt{A^2 + B^2} \sin(\gamma + \phi) = r_{tgt} \sin(\pm \lambda) - z_{tgt} \cos i, \quad (19)$$

where A is $y_{tgt} \sin i$, B is $x_{tgt} \sin i$, and ϕ is $\arctan\left(\frac{B}{A}\right)$. Because $\gamma \in [0, 2\pi]$, two γ values are obtained through Equation (19). One value of γ is a value for the ascending situation,

and the other is the value for a descending situation. Therefore, when \vec{r}_{tgt} and θ_{inc} are given, four values of \hat{h} are obtained using two values of γ and $\pm\lambda$ that determine the imaging situation.

To derive $RADN_{op}$ from the obtained \hat{h} , the geometric relationship between \hat{h} , \vec{r}_{tgt} , \vec{r}_{sat} , and $RADN_{op}$ is used, as shown in Figure 12. At $epoch_{SAR}$, \hat{h} , \vec{r}_{tgt} , and \vec{r}_{sat} are located on the same plane; therefore, the arguments of latitude (u_{SAR}) of satellite at $epoch_{SAR}$ is

$$u_{SAR} = \begin{cases} \frac{\pi}{2} + \arccos\left(\left(\hat{r}_{tgt} \times \hat{h}\right) \cdot \hat{n}_a\right), & \left(\hat{r}_{tgt} \times \hat{h}\right) \cdot \hat{K} \geq 0 \\ \frac{\pi}{2} - \arccos\left(\left(\hat{r}_{tgt} \times \hat{h}\right) \cdot \hat{n}_a\right), & \left(\hat{r}_{tgt} \times \hat{h}\right) \cdot \hat{K} < 0 \end{cases} \quad (20)$$

where \hat{r}_{tgt} is the unit vector of \vec{r}_{tgt} , and $\hat{n}_a = \hat{K} \times \hat{h}$ is the ascending node vector. Finally, $RADN_{op}$ hanged by the Earth's rotation while the satellite moved from the descending node to u_{SAR} can be obtained as in Equation (21).

$$RADN_{op} = \arccos(\hat{l}_{ECEF} \cdot \hat{n}) + \pi + \omega_E(\pi + u_{SAR})/n, \quad (21)$$

where \hat{l}_{ECEF} is the I -axis of the ECEF frame, which is the standard of longitude at $epoch_{SAR}$, and ω_E is the angular velocity of Earth's rotation, and n is mean motion of a satellite. For each of the four values of \hat{h} , four $RADN_{op}$ sectors can be obtained as the minimum and maximum θ_{inc} , as shown in Figure 10.

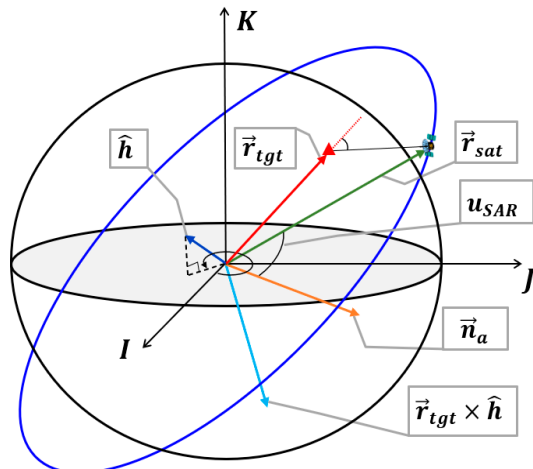


Figure 12. Geometric relationships between \hat{h} , \vec{r}_{tgt} , \vec{r}_{sat} , and $RADN_{op}$.

4.1.2. Obtaining the Precise $RADN_{op}$ Using a Numerical Method

$RADN_{op}$ calculated by the geometric method is inaccurate because it is based on a two-body problem that does not reflect perturbations such as non-spherical Earth, atmospheric drag, third body gravities (Sun, Moon), and solar radiation. $RADN_{op}$ and $epoch_{SAR}$ obtained using a geometric method for a target located in mid-latitudes generate a squint angle, the angle between the vertical plane of the satellite's velocity and the position vector of the target, of approximately 6° and θ_{inc} error of approximately 5° . This error increases as the latitude of the target increases. For the target located below the latitude of 70° , the squint angle and θ_{inc} errors were 15° and 10° or less, respectively.

To obtain accurate $RADN_{op}$ and $epoch_{SAR}$ values, numerical methods are applied in the coverage of $\pm 1.5^\circ$ and ± 40 s to the geometrically obtained $RADN_{op}$ and $epoch_{SAR}$, respectively. Here, the $\pm 1.5^\circ$ for $RADN_{op}$ makes the numerical method search approximately $\pm 10^\circ$ coverage around the geometrically calculated θ_{inc} , and the ± 40 s for $epoch_{SAR}$ makes the numerical method search approximately $\pm 20^\circ$ coverage around the geometrically calculated squint angle. The precise $RADN_{op}$ and $epoch_{SAR}$ are obtained as the values where

the squint angle and θ_{inc} errors are simultaneously minimum within the search boundary for the geometrically obtained $RADN_{op}$ and $epoch_{SAR}$.

Figure 13 shows the difference in the accuracy of $RADN_{op}$ and $epoch_{SAR}$ obtained using the geometrical method and the geometrical plus numerical method for the Science Hall of Yonsei University located at 37.56413° N, 126.93470° E. “Case No” refers to the eight situations of SAR imaging, as shown in Table 5. The accuracy of $RADN_{op}$ and $epoch_{SAR}$ is determined by the magnitude of the squint angle error and θ_{inc} error, which are differences from desired squint angle (0°) and θ_{inc} (25° or 35°) for each imaging situation, and these errors are obtained using the satellite positions propagated from the $RADN_{op}$ to the $epoch_{SAR}$ for each imaging situation. Only geometrically calculated $RADN_{op}$ and $epoch_{SAR}$ values produce a squint angle error of $4^\circ \sim 6^\circ$ and a θ_{inc} error of $2^\circ \sim 5^\circ$. However, the geometrically plus numerically obtained $RADN_{op}$ and $epoch_{SAR}$ values improve the squint angle error and the incident angle error to less than 0.1° .

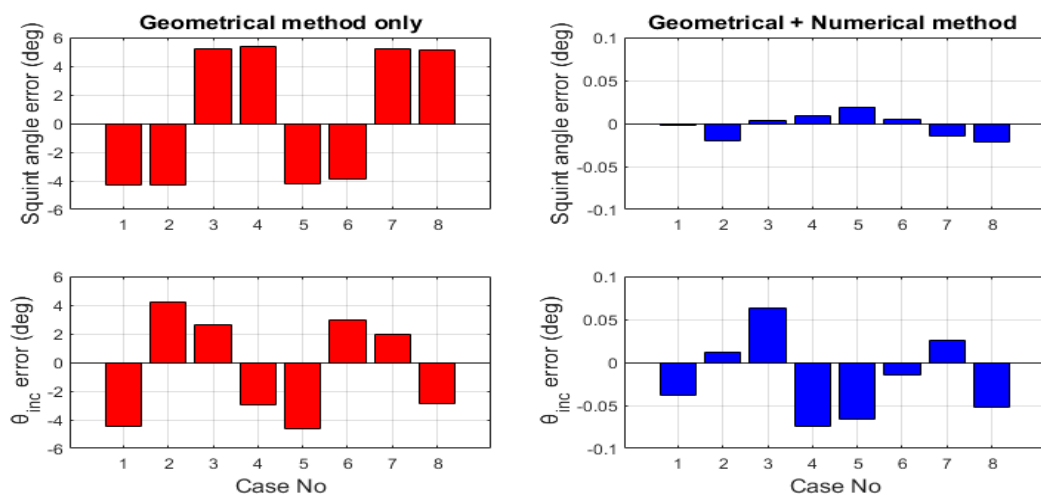


Figure 13. Difference in the accuracy of $RADN_{op}$ and $epoch_{SAR}$ obtained using the geometrical method (left) and geometrical plus numerical method (right). Squint angle error (top) and θ_{inc} error (bottom) at the $epoch_{SAR}$ of each imaging situation.

Table 5. Case number for imaging situations at $epoch_{SAR}$.

| θ_{inc} Ascend/Descend Beam Direction | Minimum | | | | Maximum | | | |
|--|------------------------------|------------------|-------------------------------|------------------|------------------------------|------------------|-------------------------------|------------------|
| | Ascending Left Looking | Right Looking | Descending Left Looking | Right Looking | Ascending Left Looking | Right Looking | Descending Left Looking | Right Looking |
| Case No | 1 | 2 | 3 | 4 | 5 | 6 | 7 | 8 |

4.2. Attitude Control Strategy for Multistatic SAR Imaging

Figure 14 shows a block diagram of the autonomous attitude-control strategy of the multistatic SAR microsatellite to which the $RADN_{op}$ concept is applied. When a satellite passes through a descending node, if it is located within the $RADN_{op}$ sector, the satellite switches itself to SAR mode. Then, the states of the satellites and the target are propagated to $epoch_{SAR}$, where SAR imaging is expected, and the precise states at $epoch_{SAR}$ are obtained. Using the relative satellites and target positions, an accurate satellite attitude for target pointing is calculated. At this time, yaw and pitch steering maneuvers are applied to remove residual Doppler shifts induced by target movements caused by the Earth's rotation. These yaw and pitch steering maneuvers are determined by the satellite's position and velocity in $epoch_{SAR}$ [36].

When the attitude calculation of the SAR mode is completed, the attitude control starts from the sun-pointing mode to the SAR-imaging mode 10 min before $epoch_{SAR}$. This lead time of 10 min is set in consideration of the time taken to change the attitude at $2^\circ/\text{s}$ or

less, time to stabilize the attitude of the satellites, the condition that the target-pointing attitude must be completed before half of the radar beam width, time to update the latest navigation data and prepare the subsystem, and the margin time.

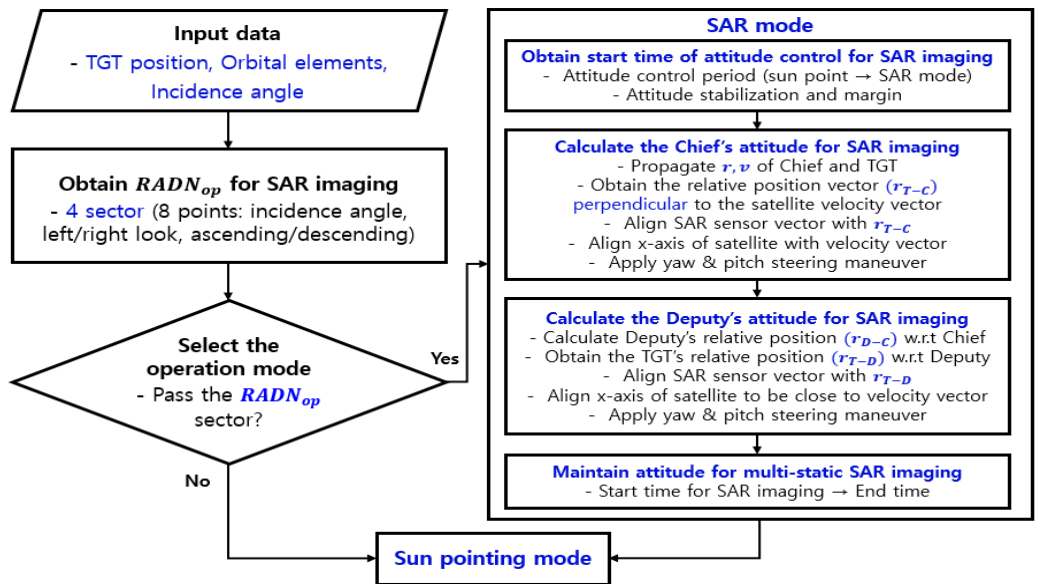


Figure 14. Flowchart of the autonomous attitude-control algorithm for multistatic SAR imaging with the $RADN_{op}$ concept applied.

4.3. Design of the Attitude-Control Algorithm

The attitude of the SAR microsatellite is controlled by a reaction wheel of a pyramid structure. The dynamics of the reaction wheel used for the attitude control of the satellite are derived from the law of angular momentum conservation as given in Equation (22) [37].

$$\vec{T}_d = \dot{\vec{H}} + \vec{\omega} \times \vec{H}, \quad (22)$$

where \vec{T}_d is the disturbance torque, $\vec{\omega}$ is the angular velocity of the satellite, and \vec{H} is the angular momentum of the satellite. Here, \vec{H} can be expressed by dividing the angular momentum of the reaction wheel and the angular momentum of the satellite excluding the reaction wheel as in Equation (23).

$$\vec{H} = I\vec{\omega} + \vec{h}_{rw}, \quad (23)$$

where, I is the tensor of inertia of the satellite and \vec{h}_{rw} is the angular momentum of the reaction wheels.

Substituting Equation (23) into Equation (22) and applying a small value approximation to remove the stiffness caused by the rotation of each wheel, a simple equation of motion is derived as [37]

$$\vec{T} = I\ddot{\vec{q}} + \dot{\vec{h}}_{rw}, \quad (24)$$

where \vec{T} is the control torque, and \vec{q} is quaternion vector, $\vec{q} = [q_1 \ q_2 \ q_3]^T$, that excludes q_4 from quaternion q . To control the attitude of the satellite, the variation of the angular momentum of the wheel \vec{h}_{rw} must be appropriately adjusted; $\dot{\vec{h}}_{rw}$ applied with a simple and reliable PD controller is

$$\dot{\vec{h}}_{rw} = K \left(\vec{q} + C_t \dot{\vec{q}} \right), \quad (25)$$

where K is the control gain, and C_t is the time constant. By substituting Equation (25) into Equation (24), the equation of motion of the attitude control can be obtained as Equation (26) [37].

$$I \ddot{\vec{q}} + KC_t \dot{\vec{q}} + K \vec{q} = \vec{T}, \quad (26)$$

K and C_t can be calculated as shown in Equation (27), by applying the final-value theorem to the transfer function of Equation (26) [37].

$$K_i \geq \frac{T_i}{q_{i,dss}}, \quad C_{t,i} = \frac{2\epsilon_i}{\sqrt{K_i/I_i}} \quad (27)$$

where $i = 1, 2, 3$ means each axis of the body frame, $q_{i,dss}$ is the desired steady-state error of each quaternion, and ϵ is a damping ratio [37].

4.4. Numerical Simulations of Autonomous Attitude Control

This section verifies the attitude control algorithm of multistatic SAR microsatellites through simulations of SAR mode maneuvers for VHRSI. The simulations are performed from the moment the chief satellite is located in the $RADN_{op}$ sector to the time when the multistatic SAR imaging mode is completed. The conditions for the orbital dynamics model and orbit determination are shown in Tables 3 and 4, and the other conditions for the attitude control simulation are shown in Table 6. Here, the specifications of the star tracker, VST-68M of VECTRONIC Aerospace inc., and the reaction wheel, NRWA-T065 of New space inc., with a heritage for microsatellites, are applied [38,39].

Table 6. Simulation conditions of attitude control for multistatic SAR microsatellites.

| | Contents | Specifications |
|----------------|-----------------------------|--|
| Satellite | Tensor of inertia | $\begin{bmatrix} 3.66 & 0.48 & -0.78 \\ 0.19 & 24.92 & 1.10 \\ -0.02 & 0.96 & 32.05 \end{bmatrix} \text{ kg}\cdot\text{m}^2$ |
| | Control rate | 1 Hz |
| | Maximum angular velocity | $2^\circ/\text{s}$ |
| | Average disturbance torque | 0.001 mN·m (1σ) |
| Star tracker | Accuracy | 5 arcsec (2σ) |
| | Update rate | 5 Hz |
| Reaction wheel | Maximum torque | 20 mN·m |
| | Maximum angular momentum | 0.65 N·m·s |
| | Wheel speed range | ± 9000 rpm |
| | Control accuracy | $\langle 1 \text{ rpm} @ \rangle 100 \text{ rpm}$ |
| | Skew angle (β) | 35° |
| | Rotation angle (θ) | 45° |

Figure 15 denotes the Euler angle with respect to the ECI frame (a) and the angular velocity (b) of the chief satellite during the attitude control scenario for the multistatic SAR mode. In the sun-pointing mode section, the roll and pitch angles were kept constant with the $-z$ -axis of the satellite body frame facing the sun, and the yaw angle was rotated to keep the x -axis close to the velocity vector of the satellite. In SAR mode, after maneuvering to a target-pointing attitude for stripmap mode imaging, the attitude was held constant until the end of SAR imaging. The angular velocity was maintained within the maximum limit of $2^\circ/\text{s}$.

Figure 16 shows the simulation result of the SAR mode attitude control of the chief SAR microsatellite. The value of $epoch_{SAR}$ is 3494 elapsed seconds. The SAR mode maneuver starts at 2894 s, 10 min before $epoch_{SAR}$, and the SAR antenna pointing error converges within the requirement of 0.01° at 3130 s, 4 min after the start of the SAR mode maneuver. A return maneuver for sun pointing is performed at 3523 s, 30 s after the completion of SAR imaging. The total pointing and angular velocity errors after stabilization for each

multistatic SAR satellite are shown in Table 7. For all three satellites, attitude control suitable for the operation mode was performed autonomously, and both the total pointing error requirement of 0.01° (3σ) and angular velocity error requirement of $0.0007^\circ/\text{s}$ (3σ) were satisfied.

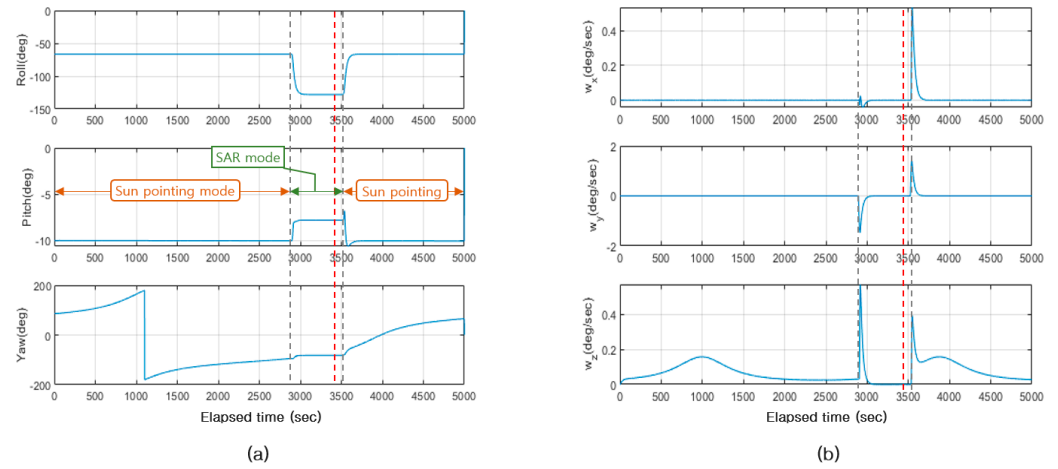


Figure 15. Attitude control simulation results: Euler angle with respect to the ECI frame (a) and angular velocity (b) of chief satellite. The red dotted line represents $\text{epoch}_{\text{SAR}}$.

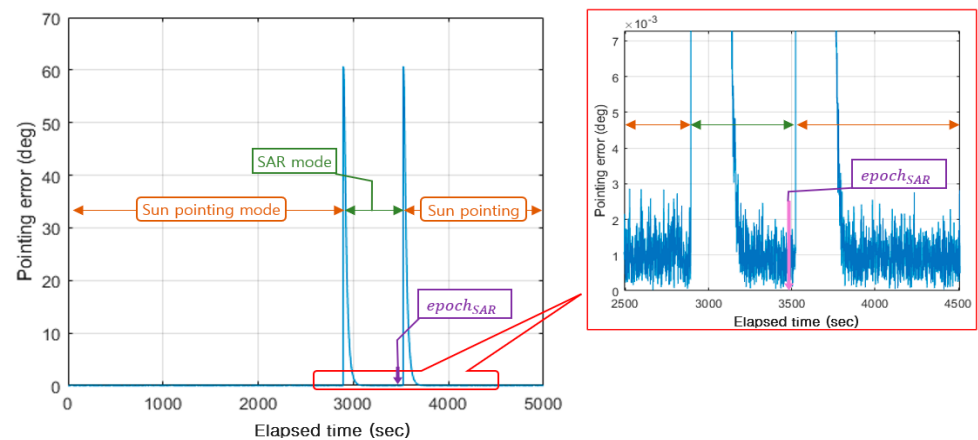


Figure 16. Attitude control simulation result: total pointing error of the chief satellite.

Table 7. Attitude control accuracy of SAR mode.

| | Leader Deputy | Chief | Trailer Deputy |
|--------------------------------------|--------------------------|--------------------------|--------------------------|
| Total pointing error (3σ) | 0.00328° | 0.00332° | 0.00320° |
| Angular velocity error (3σ) | $0.00015^\circ/\text{s}$ | $0.00016^\circ/\text{s}$ | $0.00016^\circ/\text{s}$ |

During the autonomous multistatic SAR mode maneuver, each wheel's control torque and accumulated angular momentum are maintained within the maximum torque limit of 20 mN·m and momentum limit of 0.65 N·s, respectively. Because the difference in the attitude of the deputy satellites with respect to the chief satellite is within 50 arcsec for performing the mission scenario, the difference in the graphs of the torque and momentum of each wheel is negligibly small. Therefore, we only present graphs of the chief satellite. Through the above simulation results, the performance of the autonomous attitude control algorithm of the multistatic SAR satellite for VHRSI was verified. Using the $RADN_{op}$ concept, the satellite switched itself to the SAR mode, and attitude control that satisfies the requirements was performed in each operation mode.

5. Performance Verification and Image Analysis of a Multistatic SAR System for VHRSI

This section analyzes the qualities of SAR images obtained by the designed multistatic SAR formation system. The quality of the SAR image is degraded by various causes, such as antenna performance and beam pointing error. Therefore, when designing the SAR system, analyzing the image that reflects factors that can degrade the SAR image is required [34]. In the case of a multistatic SAR system in which a transmitter and a receiver are separated, an image analysis process for the relative position and attitude of each satellite must be performed in addition to the factors that a monostatic SAR system must consider [1]. The multistatic SAR image is analyzed through an impulse response function (IRF) for a point target that can measure various image quality parameters [15]. In addition, the range and azimuth profiles, which represent the amplitude of the received signal in the range and azimuth directions based on the center of the point target of the IRF, can explain the spatial resolution, Peak sidelobe ratio (PSLR), and Integrated sidelobe ratio (ISLR) of the SAR images. Here, the resolution of the SAR image is obtained as an impulse response width (IRW), the main-lobe width at -3 dB, of the range and azimuth profile [4].

Tables 2–4 and 6 are applied to the simulation conditions of multistatic SAR imaging, and the location of the point target is 37.56413° N, 126.93470° E. Here, a point target is applied because several important factors related to SAR image quality can be estimated from the point target response [4]. The initial position of the chief SAR microsatellite is the center point of the ascending and left-looking $RADN_{op}$ sector. In this case, $RADN_{op}$ is 251.2° , $epoch_{SAR}$ is 3494 s, and the incidence angle θ_{inc} is 27.5° . The multistatic SAR imaging simulation process is done with a polar format algorithm (PFA). The PFA forms the SAR image by interpolating SAR data existing on an orthogonal grid in digital data space to reflect the spectral support of an actual SAR signal. The interpolated SAR data can be applied to a two-dimensional inverse fast Fourier transform, which can reduce the computational load of SAR imaging [40,41]. Additionally, PFA is widely used for bistatic SAR imaging because there is no geometric constraint between a transmitter and receiver [40].

5.1. Performance Analysis of the Preliminary Design of a Multistatic SAR System

In Section 2, a multistatic SAR formation for VHRSI was designed as the along-track formation with a baseline of 6 km. To confirm the SAR image performance of the multistatic SAR system, images of the point target were analyzed when there was no error in determining and controlling the orbit and attitude. Subsequently, images were analyzed in a situation where the relative orbit and attitude control algorithm designed in Sections 3 and 4 were reflected.

5.1.1. Case of the Designed Orbit Path without Navigation and Attitude Errors

This section validates the resolution enhancement ability of the multistatic SAR formation system and analyzes the effect of geometric conditions such as the low Earth orbit environment and Earth rotation on multistatic SAR images. For this, the IRF of the multistatic and monostatic SAR systems for the point target are simulated and compared. Here, it is assumed that there are no navigation and attitude errors to reflect only geometric conditions.

Figures 17 and 18 denote the SAR imaging simulation results for the point target with a multistatic SAR system for VHRSI and a monostatic SAR system with only the chief satellite under designed orbit conditions, respectively. With each IRF image of the point target, it is confirmed that both systems imaged the point target precisely at the center of the orthogonal grid of target-centric digital data space using a polar format algorithm. Moreover, it is verified that the image resolution of the multistatic SAR system is improved by comparing the image cell size. The range resolutions of both systems are 0.93 m, which satisfies the requirement. However, multistatic SAR has improved in terms of PSLR and ISLR. The azimuth resolutions are 1.14 m and 1.61 m for multistatic SAR and monostatic SAR, respectively. Through this, it was verified that the multistatic SAR system for VHRSI improves the azimuth resolution. However, the SAR image obtained by the theoretically designed multistatic SAR formation does not satisfy the azimuth resolution requirement.

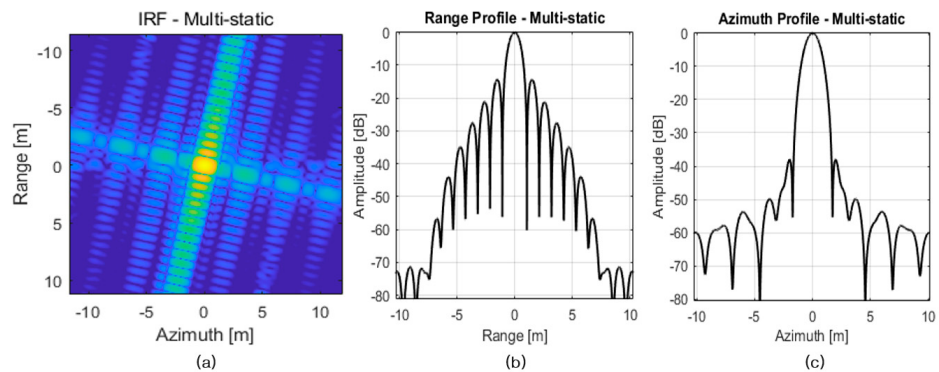


Figure 17. Multistatic SAR imaging simulation results under a 6 km baseline and designed orbit condition: IRF (a), range profile (b), and azimuth profile (c).

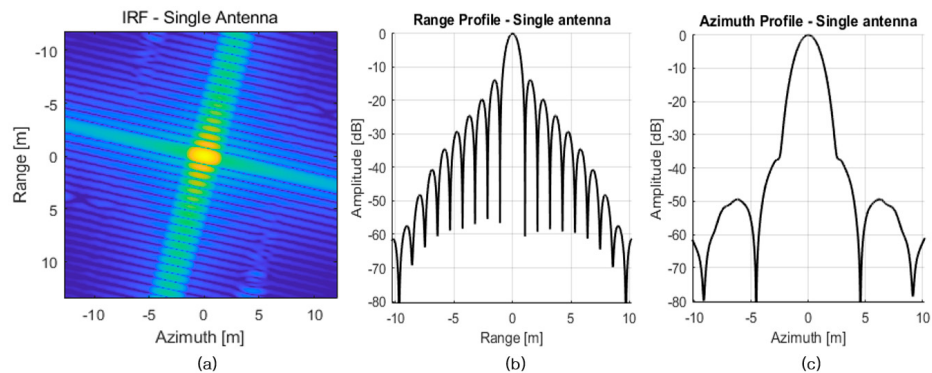


Figure 18. Monostatic SAR imaging simulation results under the designed orbit condition: IRF (a), range profile (b), and azimuth profile (c).

5.1.2. Case of the Determined Orbit Path with Navigation and Attitude Errors

The three multistatic SAR satellites inevitably experience various navigation and attitude errors, such as absolute and relative orbit determination and control errors and attitude determination and control errors.

Figure 19 denotes the simulation results imaged for the point target with a multistatic SAR system for VHRSI with determined orbit conditions. The algorithms designed in Sections 3 and 4 perform relative orbit and attitude control, and the conditions related to navigation and attitude are reflected in Tables 3, 4 and 6. When imaging was performed in the same process as in the designed orbit case, the target image was not created in the center of the digital data grid. Moreover, the positions of the targets imaged by each SAR microsatellite were all separated in the digital data grid. This phenomenon implies a loss of the resolution enhancement capability of multistatic SAR systems.

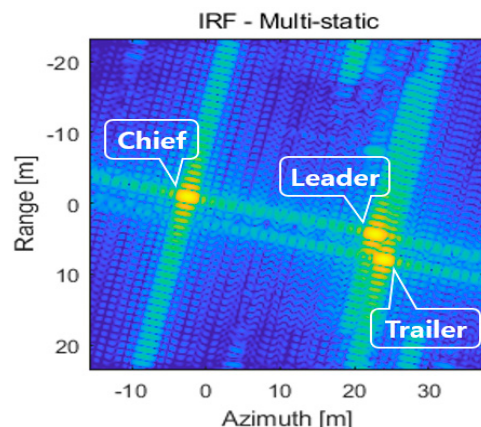


Figure 19. Point target IRF of a multistatic SAR system in the case of a baseline of 6 km and determined orbit.

5.1.3. Analysis of the Target Image-Separation Phenomenon Due to Navigation and Attitude Errors

To find the reason for the target image-separation phenomenon in the determined orbit condition, the characteristics of the signal were analyzed during the SAR imaging process. From the analysis, it was confirmed that there was a phase error even after the signal compression process was completed when the navigation and attitude errors were reflected. In the normal SAR imaging process, the signal phase is constant after the signal compression is completed. In fact, these uncompensated phase errors degrade the quality of the SAR images [42,43].

Figure 20 shows the phase difference between the signals received under determined and designed orbit conditions. Under the designed orbit condition ignoring the navigation and attitude errors, the phase of the received signal to the point target is constant. However, under the determined orbit condition, reflecting navigation and attitude errors, it is confirmed that the phase error increases almost linearly in both the fast-time frequency domain for range direction and slow-time domain for the azimuth direction. Therefore, any phase error component that is not a constant within the IRF can contribute to navigation and attitude errors. This phase error can be directly estimated from the IRF formed after a rough focusing and can be filtered by applying a phase multiplier over the raw data. Here, the phase multiplier is constructed from the estimated phase error [43]. In this way, an algorithm for correcting the phase error due to navigation and attitude errors is presented.

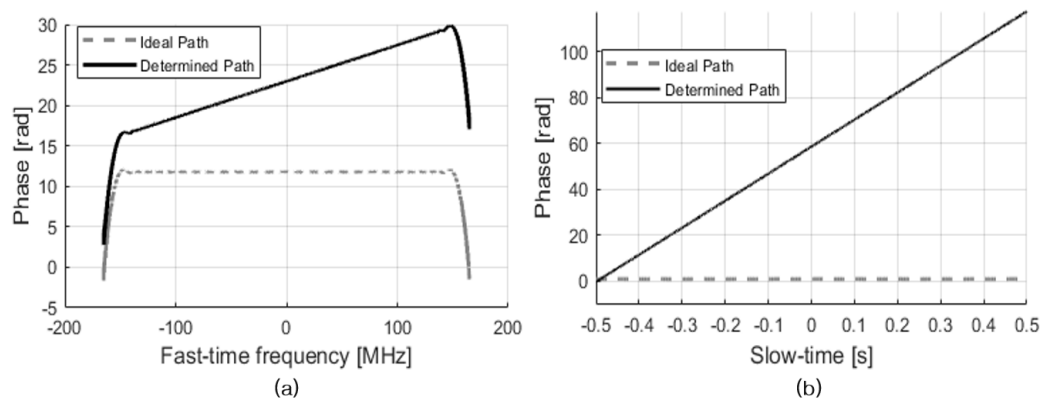


Figure 20. Phases of the received signal that has completed signal compressions in the range and azimuth directions. Fast-time frequency domain for the range direction (a) and slow-time domain for the azimuth direction (b). The solid and dotted lines represent the phase of the received signal under the determined and designed orbits, respectively.

5.1.4. Multistatic SAR Imaging with a Phase-Correction Algorithm under the Determined Orbit Path

In the previous section, a phase-correction algorithm was presented to eliminate the target image separation phenomenon due to navigation and attitude errors, and it was added to the multistatic SAR imaging process. Imaging simulation, employing the phase-correction algorithm, of the preliminary designed multistatic SAR system is performed under the determined orbit path condition.

Figure 21 illustrates the multistatic SAR imaging simulation results of the point target with a phase-correction algorithm applied under determined orbit conditions. Consequent to correcting the phase error of each SAR antenna caused by the navigation and attitude errors using the phase-correction algorithm, the target images of all antennas were centered in the digital data grid. This means that the signal for the point target received by each antenna is well synthesized; therefore, the IRF is very similar to the results achieved under designed orbit conditions. The spatial resolution of the multistatic SAR image reflecting the phase-correction algorithm is 0.94×1.17 m, which degraded by approximately 1×4 cm, compared to the spatial resolution of designed orbit conditions, 0.93×1.14 m. However,

the spatial resolution of the preliminary designed multistatic SAR system could not satisfy the 1 m requirement.

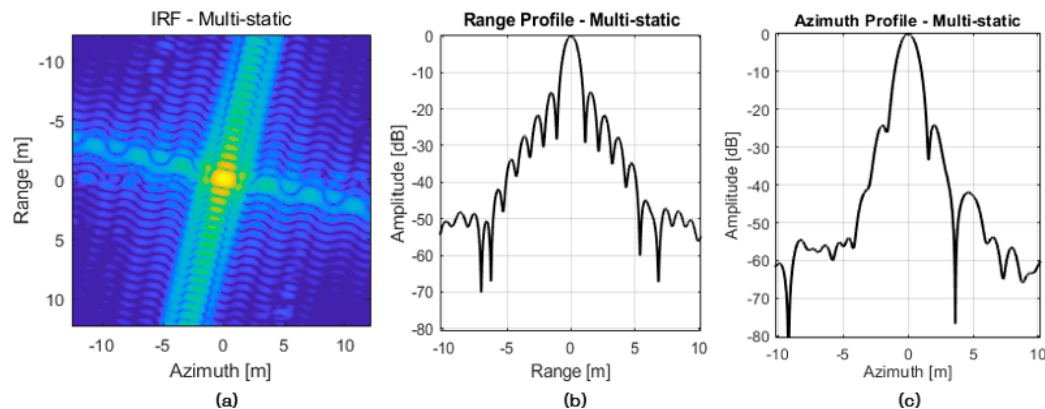


Figure 21. Multistatic SAR imaging simulation results reflecting the phase-correction algorithm in the case of a baseline of 6 km and a determined orbit. IRF (a), range profile (b), and azimuth profile (c).

5.2. Design Change of the Multistatic SAR System to Satisfy the Spatial Resolution Requirement

The spatial resolution of the preliminary designed multistatic SAR system is 0.94×1.17 m. The range resolution satisfies the very-high spatial resolution requirement, but the azimuth resolution does not. Therefore, the multistatic SAR formation system must be modified to have an azimuth resolution of less than 1 m. The azimuth resolution can be improved by increasing L_{SA} according to Equation (2). Increasing L_{SA} can be achieved by increasing the baseline between the satellites.

Figure 22 denotes the azimuth profiles of the point target according to different baselines for the improvement of the azimuth resolution. The results for the azimuth resolution and PSLR for four cases are in Table 8. As the baseline becomes longer, the azimuth resolution improves, and the submeter azimuth resolution can be achieved when the baseline is 7.5 km or more.

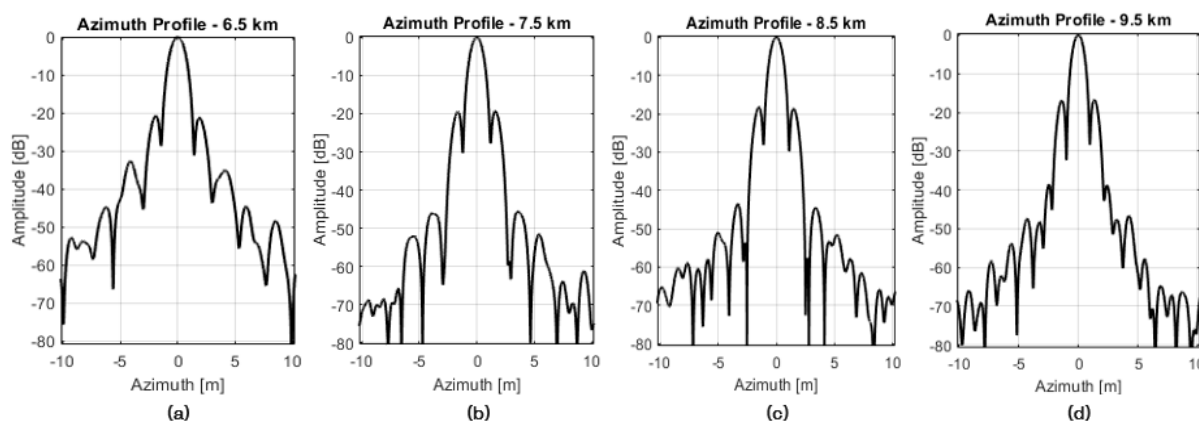


Figure 22. Azimuth profile with respect to the various baselines: 6.5 km (a), 7.5 km (b), 8.5 km (c), 9.5 km (d).

Table 8. Azimuth resolution and PSLR with respect to the baseline.

| | 6.5 km | 7.5 km | 8.5 km | 9.5 km |
|------------------------|--------|--------|--------|--------|
| Azimuth resolution (m) | 1.125 | 0.962 | 0.891 | 0.815 |
| PSLR (dB) | -20.8 | -19.3 | -18.3 | -16.7 |

It should not be overlooked that the PSLR of the multistatic SAR image increases as the baseline increases because when the PSLR is high, the sidelobe affects the signal from a

close target and makes it difficult to identify close targets. The PSLR of the X-band SAR microsatellite generally considers $-15\text{--}-17$ dB or less as an appropriate level. Currently, the PSLR of the ICEYE-X2 satellite, which is representative of the commercial X-band SAR microsatellite, is also set at -17 dB [29]. If the PSLR of the multistatic SAR microsatellite for VHRSI is set to -17 dB, the baseline should be 9 km or less.

An additional consideration in selecting the baseline is that the Doppler bandwidth of the signal received from each antenna should be continuous. For this, the baseline should not exceed the azimuth beam width of the SAR antenna. The length of the antenna of the multistatic SAR satellite for VHRSI is 2.2 m, and the footprint of the beam in the azimuth direction is 9.8 km [27]. Therefore, if the baseline exceeds 9.8 km, the effect of improving the resolution through a multistatic SAR system is lost. The baseline is set to 7.5 km, considering factors for baseline setting and relative orbit control error. Accordingly, the changed synthetic aperture diameter is 24.3 km, which is 3 km longer than the preliminary design.

Figure 23 is the SAR imaging simulation result of the point target using the final designed multistatic SAR system for VHRSI. The absolute orbit determination, relative orbit determination, relative orbit control, and beam pointing errors are 2 m (1σ), 0.1 m (1σ), 100 m (1σ), and 0.005° (3σ), respectively. A phase-correction algorithm was applied. The received signal for the point target obtained by three separate antennas is well imaged in an image cell smaller than 1 m located on the center point of the digital data grid. The spatial resolution of the finally designed multistatic SAR system is 0.95×0.96 m, which satisfies the very-high spatial resolution requirement.

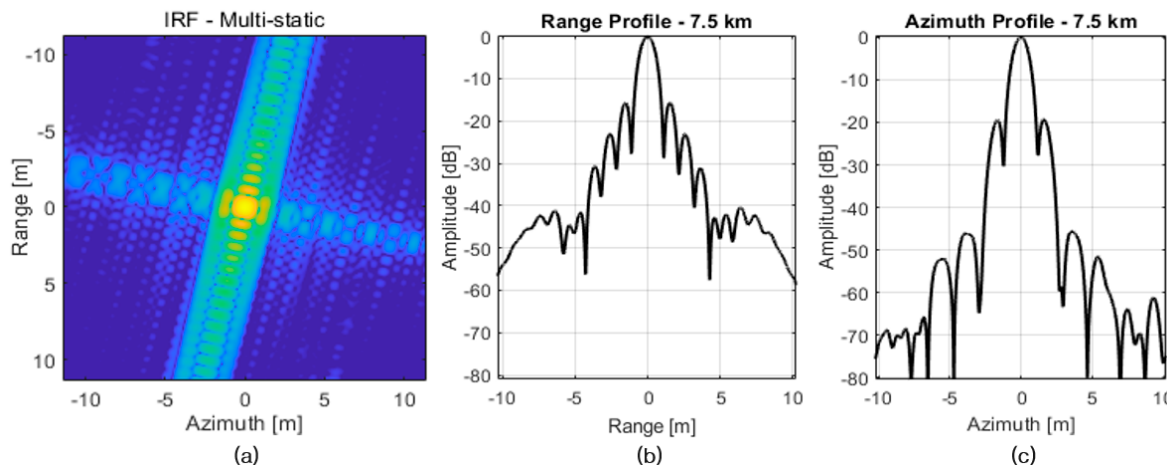


Figure 23. Imaging simulation results of the final designed multistatic SAR system, IRF (a), range profile (b), and azimuth profile (c).

5.3. Analysis of the Multistatic SAR Image with Respect to Navigation and Beam Pointing Errors

The performance of navigation and attitude control of the finally designed multistatic SAR satellites is the result of reflecting the almost top specification of the recently operated COTS component. Because navigation and attitude control performance may be degraded by various causes, it is necessary to analyze the error range of navigation and attitude control that can satisfy the resolution requirements. This analysis can establish detailed requirements for navigation and attitude.

5.3.1. SAR Image Analysis According to the Relative Orbit Determination Error

Figure 24 shows the range and azimuth profiles according to the relative position determination error (1σ) between SAR microsatellites. When the relative orbit determination error is less than 1 m, the change in range and azimuth resolutions due to the relative orbit determination error is negligible. However, when the relative orbit determination error was 1 m, it was confirmed that the range and azimuth resolutions degraded by approximately 1%. Through this, it is concluded that resolution degradation occurs when the relative position determination error is larger than the resolution. In fact, when the multistatic SAR

imaging simulation was performed by reflecting a relative orbit determination error of 1.5 m, the point target was separated and distorted on the IRF. Therefore, it is appropriate to set the relative orbit determination error of the multistatic SAR system for VHRSI to 1 m or less.

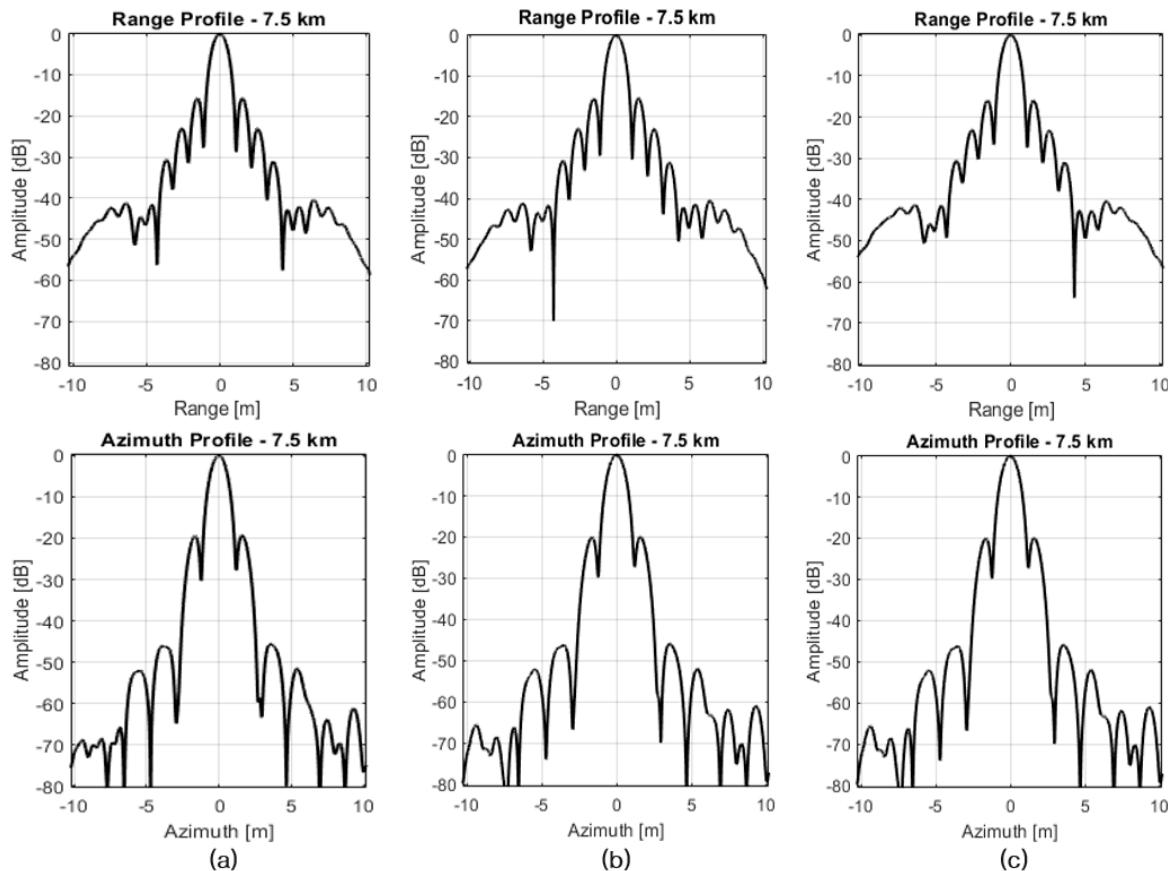


Figure 24. Range profile (**top**) and azimuth profile (**bottom**) with respect to the relative orbit determination error, 0.1 m (**a**), 0.5 m (**b**), and 1.0 m (**c**).

5.3.2. SAR Image Analysis According to the Relative Orbit Control Error

Relative orbit control errors cause changes in the baseline between SAR microsatellites. Because the baseline variations change the azimuth resolution, the requirement of the relative orbit control error should be set within the boundary that can satisfy the very-high-resolution requirement. The resolution of the multistatic SAR image according to the relative orbit control error can be analyzed using data in Table 8 and Figure 22. If the baseline is within 7.3 km, the azimuth resolution becomes worse than 1 m. Conversely, if the baseline exceeds 9.8 km, the azimuth resolution improvement effect through the multistatic system is lost. Additionally, to keep the PSLR below -17 dB, the baseline should be less than 9 km. Therefore, the relative orbit control error of the multistatic SAR formation system for VHRSI that satisfies the resolution requirement is to keep the baseline within $-200\sim+1500$ m.

5.3.3. SAR Image Analysis According to the Absolute Orbit Determination and Attitude Control Errors

To analyze the spatial resolution change according to the absolute orbit determination error, a multistatic SAR imaging simulation was performed by reflecting the 2 m, 5 m, and 10 m (1σ) absolute orbit determination errors for all SAR microsatellites. According to the simulation results, the spatial resolution or PSLR did not change by more than 1% due to the absolute orbital error. In the case of satellite navigation using a GPS, the orbit determination error does not exceed 10 m (1σ).

In the case of the attitude control error, the multistatic SAR imaging simulation was performed for the case where the attitude control error for each axis of all SAR microsatellites was 0.005° , 0.01° , and 0.02° (1σ). Consequently, no significant change of more than 1% could be confirmed in the spatial resolution or PSLR. No further simulations were performed because the attitude control error generally does not exceed 0.02° (1σ) for the SAR microsatellites.

5.4. Performance Verification of the Multistatic SAR System through Near-Multi-Target Imaging Simulation

To finally verify the performance of the multistatic SAR system for VHRSI, a multistatic SAR imaging simulation was performed for multiple targets spaced 1.5 m apart. The multistatic SAR imaging simulation for near-multi-targets is performed to confirm the ability to identify multiple targets at close range, which is limited by point-target image analysis. Figure 25 denotes the simulation results of SAR imaging for near-multi-targets of a multistatic SAR system (a) and a monostatic SAR system (b). Through the result of the multistatic SAR system in Figure 25a, it can be confirmed that the target's image at an interval of 1.5 m is separated and identified. Conversely, in the case of a monostatic SAR system, two targets in the azimuth direction interfered with each other and were crushed like one target. In this case, target identification is impossible. The resolution enhancement function of the multistatic SAR system is verified through the simulation results of SAR imaging for near-multi-targets.

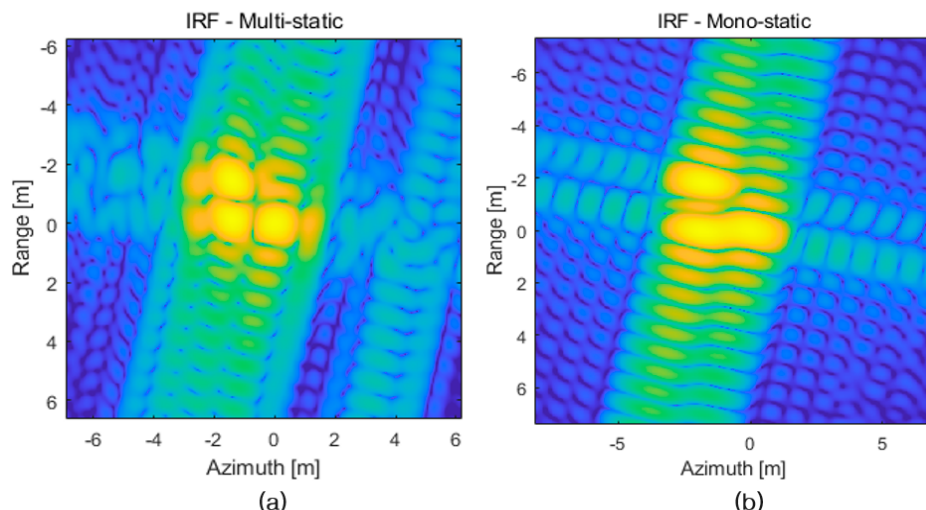


Figure 25. Near-multi-target imaging simulation results of a multistatic SAR system (a) and monostatic system (b).

6. Conclusions

For continuous very-high-resolution SAR imaging, we designed a multistatic SAR formation-flying system that enables very-high-resolution SAR imaging in stripmap mode using the concept of multistatic SAR. This study presents a multistatic SAR formation-flying system for VHRSI, autonomous relative orbit, and attitude control algorithm for the operation of a multistatic SAR system, and it verifies the performance of the multistatic SAR formation system through SAR imaging simulations. The formation flying system based on the theory of SAR image resolution was designed such that three SAR microsatellites maintained a baseline of 6 km in the along-track direction. Subsequently, the baseline was finally modified to 7.5 km through multistatic SAR imaging simulations. An autonomous relative orbit control algorithm was designed to maintain the baseline of the multistatic SAR satellites using relative orbital elements. Subsequently, it was verified that the relative position error was maintained within 45 m (3σ) through the relative orbit control simulation. An autonomous attitude-control algorithm was designed by applying the $RADN_{op}$

sector concept to enable SAR microsatellites to switch to SAR mode by themselves. After the autonomous attitude-control simulation, the satellites performed attitude maneuvers suitable for the operation mode and maintained the pointing error within 0.0035° (3σ). The autonomous attitude-control algorithm applying the optimal RADN sector concept can contribute to the efficient operation of multiple Earth observation satellites. SAR imaging simulation was performed to verify the resolution improvement performance of the designed multistatic SAR system. The spatial resolution of the developed multistatic SAR system for VHRSI was 0.95×0.96 m, which satisfied the resolution requirements. The multistatic SAR formation-flying system developed in this study is meaningful in that it can obtain very-high-resolution SAR images over a wide area using inexpensive and simple SAR microsatellites. Moreover, the multistatic SAR concept for resolution enhancement can be applied by adding receive-only satellites to the currently operating SAR satellite. The multistatic SAR formation-flying system for VHRSI can greatly improve the very-high-resolution Earth observation area. As a future work, there is a study to improve the accuracy of RADN obtained by geometric method and equation of attitude motion. If the accuracy of the RADN obtained by the geometric method is improved, the computational efficiency will increase because the range to be calculated by the numerical method is reduced. The accuracy of the attitude controller can be improved by increasing the accuracy of the attitude dynamics by reflecting gyroscopic torque compensation.

Author Contributions: Conceptualization, S.L., J.K. and S.-Y.P.; methodology, S.L.; software, S.L. and J.K.; validation, S.L. and J.K.; formal analysis, S.L.; investigation, S.L. and J.K.; resources, M.-H.K. and S.-Y.P.; data curation, S.L. and J.K.; writing—original draft preparation, S.L.; writing—review and editing, M.-H.K. and S.-Y.P.; visualization, S.L.; supervision, S.-Y.P.; project administration, S.L. and Y.S.; funding acquisition, Y.S. All authors have read and agreed to the published version of the manuscript.

Funding: This work was supported by major research funding from Hanwha System (grant number: C-19-010-1).

Data Availability Statement: Not applicable.

Conflicts of Interest: The authors declare no conflict of interest. The funders had no role in the design of the study; in the collection, analyses, or interpretation of data; in the writing of the manuscript; or in the decision to publish the results.

References

1. D'Errico, M. *Distributed Space Missions for Earth System Monitoring*; Springer: Berlin/Heidelberg, Germany, 2013.
2. Werninghaus, R.; Buckreuss, S. The TerraSAR-X mission and system design. *IEEE Trans. Geosci. Remote Sens.* **2010**, *48*, 606–614. [[CrossRef](#)]
3. Naftaly, U.; Levy-Nathansohn, R. Overview of the TECSAR satellite hardware and mosaic mode. *IEEE Geosci. Remote Sens. Lett.* **2008**, *5*, 423–426. [[CrossRef](#)]
4. Cumming, I.G.; Wong, F.H. *Digital Processing of Synthetic Aperture Radar Data*; Artech House: London, UK, 2005.
5. Castillo, J.; Younis, M.; Krieger, G. A HRWS SAR System Design with Multi-beam Imaging Capabilities. In Proceedings of the 14th European Radar Conference, Nuremberg, Germany, 11–13 October 2017; pp. 179–182. [[CrossRef](#)]
6. Javali, A.; Gupta, J.; Sahoo, A. A review on synthetic aperture radar for earth remote sensing: Challenges and opportunities. In Proceedings of the 2nd International Conference on Electronics and Sustainable Communication Systems (ICESC), Coimbatore, India, 4–6 August 2021; pp. 596–601. [[CrossRef](#)]
7. Wiley, C.A. Synthetic aperture radars—a paradigm for technology evolution. *IEEE Trans. Aerosp. Electron. Syst.* **1985**, *21*, 440–443. [[CrossRef](#)]
8. Park, T.Y.; Kim, S.Y.; Yi, D.W.; Jung, H.Y.; Lee, J.E.; Yun, J.H.; Oh, H.U. Thermal design and analysis of unfurlable CFRP skin based parabolic reflector for spaceborne SAR antenna. *Int. J. Aeronaut. Space Sci.* **2021**, *22*, 433–444. [[CrossRef](#)]
9. Gens, R.; Van Genderen, J.L. Review article SAR interferometry—issues, techniques, applications. *Int. J. Remote Sens.* **1996**, *17*, 1803–1835. [[CrossRef](#)]
10. Heer, C.; Fischer, C.; Schaefer, C. Spaceborne SAR Systems and Technologies. In Proceedings of the 2010 IEEE MTT-S International Microwave Symposium, San Diego, CA, USA, 23–28 May 2010; pp. 538–541. [[CrossRef](#)]
11. Paek, S.W.; Balasubramanian, S.; Kim, S.; de Weck, O. Small-satellite synthetic aperture radar for continuous global biospheric monitoring: A review. *Remote Sens.* **2020**, *12*, 2546. [[CrossRef](#)]
12. Grasso, M.; Renga, A.; Fasano, G.; Graziano, M.D.; Grassi, M.; Moccia, A. Design of an end-to-end demonstration mission of a Formation-Flying Synthetic Aperture Radar (FF-SAR) based on microsatellites. *Adv. Space Res.* **2021**, *67*, 3909–3923. [[CrossRef](#)]

13. Peral, E.; Im, E.; Wye, L.; Lee, S.; Tanelli, S.; Rahmat-Samii, Y.; Horst, S.; Hoffman, J.; Yun, S.H.; Imken, T.; et al. Radar technologies for earth remote sensing from CubeSat platforms. *Proc. IEEE* **2018**, *106*, 404–418. [[CrossRef](#)]
14. Sandau, R.; Roser, H.P.; Valenzuela, A. *Small Satellite Missions for Earth Observation: New Developments and Trends*; Springer: London, UK, 2010.
15. Fang, T.; Deng, Y.; Liang, D.; Zhang, L.; Zhang, H.; Fan, H.; Yu, W. Multichannel sliding spotlight SAR imaging: First result of GF-3 satellite. *IEEE Trans. Geosci. Remote Sens.* **2022**, *60*, 1–16. [[CrossRef](#)]
16. Tebaldini, S.; Flora, L.; Rocca, F. A Mimo Multi-Static SAR Satellite Formation for High Resolution 3D Imaging at Longer Wavelengths. In Proceedings of the IEEE International Geoscience and Remote Sensing Symposium, Brussels, Belgium, 11–16 July 2021; pp. 1086–1089. [[CrossRef](#)]
17. Seker, I.; Lavalle, M. Tomographic performance of multi-static radar formations: Theory and simulations. *Remote Sens.* **2021**, *13*, 737. [[CrossRef](#)]
18. Leng, X.; Ji, K.; Zhou, S.; Xing, X.; Zou, H. An adaptive ship detection scheme for spaceborne SAR imagery. *Sensors* **2016**, *16*, 1345. [[CrossRef](#)] [[PubMed](#)]
19. Servidua, P.A.; Espana, M. On autonomous reconfiguration of SAR satellite formation flight with continuous control. *IEEE Trans. Aerosp. Electron. Syst.* **2021**, *57*, 3861–3873. [[CrossRef](#)]
20. Obata, T.; Arai, M.; Asada, S.; Imaizumi, T.; Suzuki, Y. The autonomous system architecture of the small SAR satellite operation system and on-orbit autonomous operation experiences. In Proceedings of the 35th Annual AIAA/USU Conference on Small Satellites, Logan, UH, USA, 7–12 August 2021; Digital Commons.
21. D’Amico, S. Autonomous Formation Flying in Low Earth Orbit. Ph.D. Thesis, Delft University of Technology, Delft, The Netherlands, 2015.
22. Koenig, A.; D’Amico, S.; Lightsey, E.G. Formation Flying Orbit and Control Concept for the VISORS Mission. In Proceedings of the AIAA Scitech 2021 Forum, Virtual Event, 11–15 January 2021; p. 0423. [[CrossRef](#)]
23. Hudson, B. Synthetic Aperture Radar Concept of Operations. UK: OPEN SOURCE SATELLITE. 2021. Available online: <https://www.opensourcesatellite.org/ossat-download-synthetic-aperture-radar-concept-operations/> (accessed on 1 August 2022).
24. Soleh, M.; Nasution, A.S.; Hidayat, A.; Gunawan, H.; Widipaminto, A. Analysis of antenna specification for very high resolution satellite data acquisition through direct receiving system (DRS). *IJReSES* **2018**, *15*, 113–130. [[CrossRef](#)]
25. Singh, J. Spatial Content Understanding of Very High Resolution Synthetic Aperture Radar Images. Ph.D. Thesis, University of Siegen, Siegen, Germany, 2014.
26. Irvine, J.M. National Imagery Interpretability Rating Scales (NIIRS): Overview and Methodology. In Proceedings of the Optical Science, Engineering and Instrumentation ‘97, San Diego, CA, USA, 27 July–1 August 1997. [[CrossRef](#)]
27. MaCandless Jr, S.W.; Jackson, C.R. Principles of synthetic aperture radar. In *Synthetic Aperture Radar Marine User’s Manual*; Jackson, C.R., Apel, J.R., Eds.; United States Department of Commerce: Washington, DC, USA, 2004; pp. 1–24.
28. Dawidowicz, B.; Samczynski, P.; Smolarczyk, M.; Kuzmiuk, M. Analysis of SAR Images Quality Degradation Factors. In Proceedings of the Photonics Applications in Astronomy, Communications, Industry, and High-Energy Physics Experiments IV, Mierzejewice, Poland, 30 May–5 June 2005. [[CrossRef](#)]
29. ICEYE.com. SAR Product Guide; V4.0. Available online: <https://www.iceye-ltd.github.io/product-documentation/5.0/archive/archive/> (accessed on 15 December 2021).
30. Saito, H. Compact X Band Synthetic Aperture Radar on 100kg Small Satellite. In Proceedings of the IAA Symposium on Small Satellites for Earth Observation, Berlin, Germany, 20–24 April 2015; pp. 1653–1660, Digital Commons. [[CrossRef](#)]
31. Montenbruck, O.; Kahle, R.; D’Amico, S.; Ardaens, J.S. Navigation and control of the TanDEM-X formation. *J. Sci. Astronaut.* **2008**, *56*, 341–357. [[CrossRef](#)]
32. Vallado, D.A.; McClain, W.D. *Fundamentals of Astrodynamics and Applications*, 4th ed.; Microcosm: Torrance, CA, USA, 2013.
33. *State of the Art Report, Small Spacecraft Technology*; Ames Research Center, Small Spacecraft Systems Virtual Institute: Mountain View, CA, USA, 2021.
34. Chun, Y.S. Analysis of SAR Image Quality Degradation Due to Pointing and Stability Error of Synthetic Aperture Radar Satellite. Ph.D. Thesis, Chungnam National University, Daejeon, Republic of Korea, 2009.
35. Larson, W.J.; Werts, J.R. *Space Mission Analysis and Design*, 3rd ed.; Microcosm: Torrance, CA, USA, 2005.
36. Scharf, D.P. Analytic yaw-pitch steering for side-looking SAR with numerical roll algorithm for incidence angle. *IEEE Trans. Geosci. Remote Sens.* **2012**, *50*, 3587–3594. [[CrossRef](#)]
37. Chobotov, V.A. *Spacecraft Attitude Dynamics and Control*; Krieger Publishing Company: Malabar, FL, USA, 1991.
38. Kok, I. Comparison and Analysis of Attitude Control Systems of a Satellite Using Reaction Wheel Actuators. Ph.D. Thesis, Lulea University of Technology, Lulea, Sweden, 2012.
39. Markley, F.L.; Crassidis, J.L. *Fundamentals of Spacecraft Attitude Determination and Control*; Springer: New York, NY, USA, 2014.
40. VECTRONIC aerospace.com. V.S.T. Star Tracker, 68M Performance. Available online: <https://www.vectronic-aerospace.com/wp-content/uploads/2020/03/VAS-VST68M-DS2.pdf/> (accessed on 18 August 2022).
41. NEWSPACE SYSTEMS.com. Reaction Wheel Performance. Available online: https://www.newspacesystems.com/wp-content/uploads/2022/07/NewSpace-Reaction-Wheel_V11.2.pdf/ (accessed on 18 August 2022).

-
- 42. Rigling, B.D.; Moses, R.L. Polar format algorithm for bistatic SAR. *IEEE Trans. Aerosp. Electron. Syst.* **2004**, *40*, 1147–1159. [[CrossRef](#)]
 - 43. Doerry, A.W. *Basics of Polar-Format Algorithm for Processing Synthetic Aperture Radar Images*; Sandia National Laboratories (SNL): Livermore, CA, USA, 2012.

Disclaimer/Publisher’s Note: The statements, opinions and data contained in all publications are solely those of the individual author(s) and contributor(s) and not of MDPI and/or the editor(s). MDPI and/or the editor(s) disclaim responsibility for any injury to people or property resulting from any ideas, methods, instructions or products referred to in the content.